

# BMPR-2 gates activity-dependent stabilization of primary dendrites during mitral cell remodeling

藍原, 周平

<https://hdl.handle.net/2324/4496006>

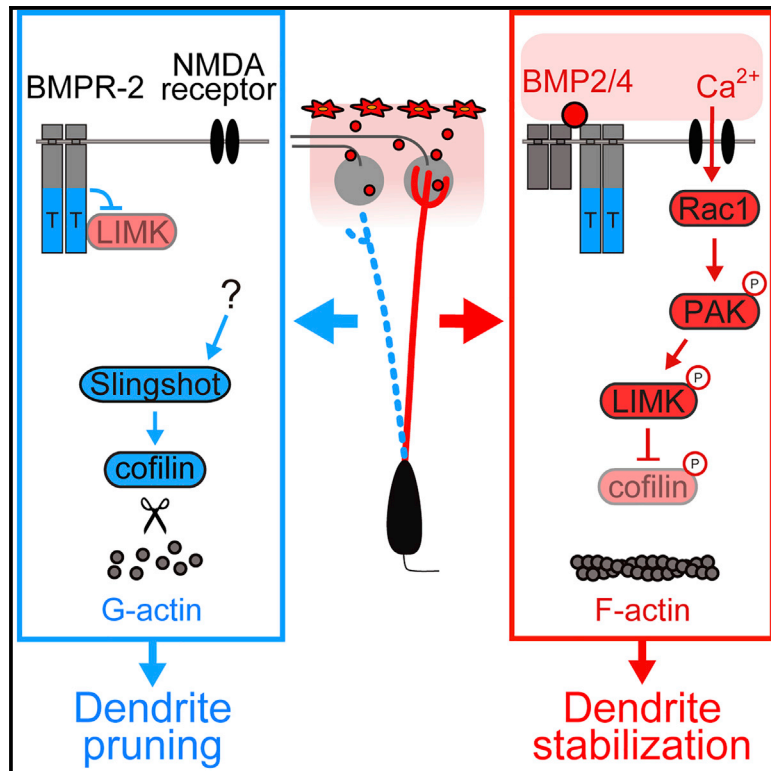
---

出版情報 : Kyushu University, 2021, 博士 (医学), 課程博士  
バージョン :  
権利関係 : (c)2021 The Author(s).



## BMPR-2 gates activity-dependent stabilization of primary dendrites during mitral cell remodeling

### Graphical abstract



### Authors

Shuhei Aihara, Satoshi Fujimoto,  
Richi Sakaguchi, Takeshi Imai

### Correspondence

imai.takeshi.457@m.kyushu-u.ac.jp

### In brief

Aihara et al. demonstrate that concomitant inputs of BMP signaling via BMPR-2 and neuronal activity via NMDAR facilitate the formation of primary dendrites within glomeruli in developing mitral cells. They also show that branch-specific stabilization of actin cytoskeleton leads to the formation of a thick primary dendrite with a tufted structure.

### Highlights

- BMPR-2 regulates selective dendrite stabilization in developing mitral cells
- Ligand-free BMPR-2 permits dendrite destabilization by inhibiting LIMK
- Ligand-bound BMPR-2 and concomitant NMDAR-Rac1-PAK-LIMK signals stabilize dendrites
- Regulation of cofilin phosphorylation and F-actin links to dendrite stability



## Article

# BMPR-2 gates activity-dependent stabilization of primary dendrites during mitral cell remodeling

Shuhei Aihara,<sup>1,2,3</sup> Satoshi Fujimoto,<sup>1,2</sup> Richi Sakaguchi,<sup>1,2,3</sup> and Takeshi Imai<sup>1,2,3,4,\*</sup><sup>1</sup>Graduate School of Medical Sciences, Kyushu University, Fukuoka 812-8582, Japan<sup>2</sup>Laboratory for Sensory Circuit Formation, RIKEN Center for Developmental Biology, Kobe 650-0047, Japan<sup>3</sup>Graduate School of Biostudies, Kyoto University, Kyoto 606-8501, Japan<sup>4</sup>Lead contact\*Correspondence: [imai.takeshi.457@m.kyushu-u.ac.jp](mailto:imai.takeshi.457@m.kyushu-u.ac.jp)<https://doi.org/10.1016/j.celrep.2021.109276>**SUMMARY**

Developing neurons initially form excessive neurites and then remodel them based on molecular cues and neuronal activity. Developing mitral cells in the olfactory bulb initially extend multiple primary dendrites. They then stabilize single primary dendrites while eliminating others. However, the mechanisms underlying selective dendrite remodeling remain elusive. Using CRISPR-Cas9-based knockout screening combined with *in utero* electroporation, we identify BMPR-2 as a key regulator for selective dendrite stabilization. *Bmpr2* knockout and its rescue experiments show that BMPR-2 inhibits LIMK without ligands and thereby permits dendrite destabilization. In contrast, the overexpression of antagonists and agonists indicates that ligand-bound BMPR-2 stabilizes dendrites, most likely by releasing LIMK. Using genetic and FRET imaging experiments, we demonstrate that free LIMK is activated by NMDARs via Rac1, facilitating dendrite stabilization through F-actin formation. Thus, the selective stabilization of primary dendrites is ensured by concomitant inputs of BMP ligands and neuronal activity.

**INTRODUCTION**

In the mammalian nervous system, functional neuronal circuits are established via a circuit remodeling process during early postnatal development. Neurons initially form excessive neurites. Later, they strengthen some neurites while eliminating others. For example, at the neuromuscular junction and the cerebellar climbing fiber-Purkinje cell synapses, multiple axons compete for one target. Although each synaptic target is initially innervated by multiple axons, only one establishes strong synapses, and all other connections are eliminated (Lichtman and Colman, 2000; Watanabe and Kano, 2011). In the barrel cortex, layer 4 neurons preferentially orient their dendrites toward thalamocortical axonal inputs through selective dendrite remodeling (Iwasato and Erzurumlu, 2018). It has been assumed that the neurite remodeling is a result of interplay between molecular guidance and activity-dependent processes (Valnegri et al., 2015; Wong and Ghosh, 2002); however, we do not fully understand how these factors orchestrate neurite remodeling. A long-standing question in the field is how some neurites are selectively strengthened and others are weakened during the remodeling process.

To study the mechanisms of selective neurite remodeling, mitral cells in the mouse olfactory bulb (OB) are an excellent model system. In the olfactory system, olfactory sensory neurons (OSNs) expressing the same type of odorant receptor converge their axons onto a set of glomeruli in the OB. OSN inputs are then relayed to the second-order neurons, mitral and tufted cells, in the glomeruli of the OB. A single glomerulus is typi-

cally innervated by 20–50 mitral/tufted cells (Imai, 2014). Each of the mitral/tufted cells connects its primary dendrite to a single glomerulus. Early in development, mitral cells extend multiple dendrites to multiple glomeruli; however, they stabilize some but destabilize other dendrites over time. By the end of the first postnatal week, they have eliminated all but one winning primary dendrite. Eventually, the winning primary dendrite forms a thick tufted structure within a glomerulus (Blanchart et al., 2006; Fujimoto et al., 2019; Lin et al., 2000; Malun and Brunjes, 1996). In general, neuronal activity plays important roles during the neurite remodeling process. However, it has remained unclear how a particular primary dendrite in a mitral cell is selectively stabilized—a process that protects dendrites from pruning—during the activity-dependent remodeling process.

In this study, we screened for cell surface receptors that control the dendrite remodeling process in mitral cells, employing CRISPR-Cas9-based knockout (KO) vectors combined with *in utero* electroporation. We found that BMPR-2 plays a critical role in selective dendrite stabilization during the remodeling process. In the absence of ligands, BMPR-2 inhibits LIM kinase (LIMK) 1 through its intracellular tail domain, which permits dendrite destabilization. However, ligand-bound BMPR-2 promotes dendrite stabilization, most likely by releasing LIMK1. Free LIMK is activated by neuronal activity via the NMDA receptor (NMDAR)-Rac1-PAK pathway, resulting in F-actin formation and dendrite stabilization. Thus, dendrites are selectively stabilized when bone morphogenetic protein (BMP) ligands and glutamatergic inputs co-exist.



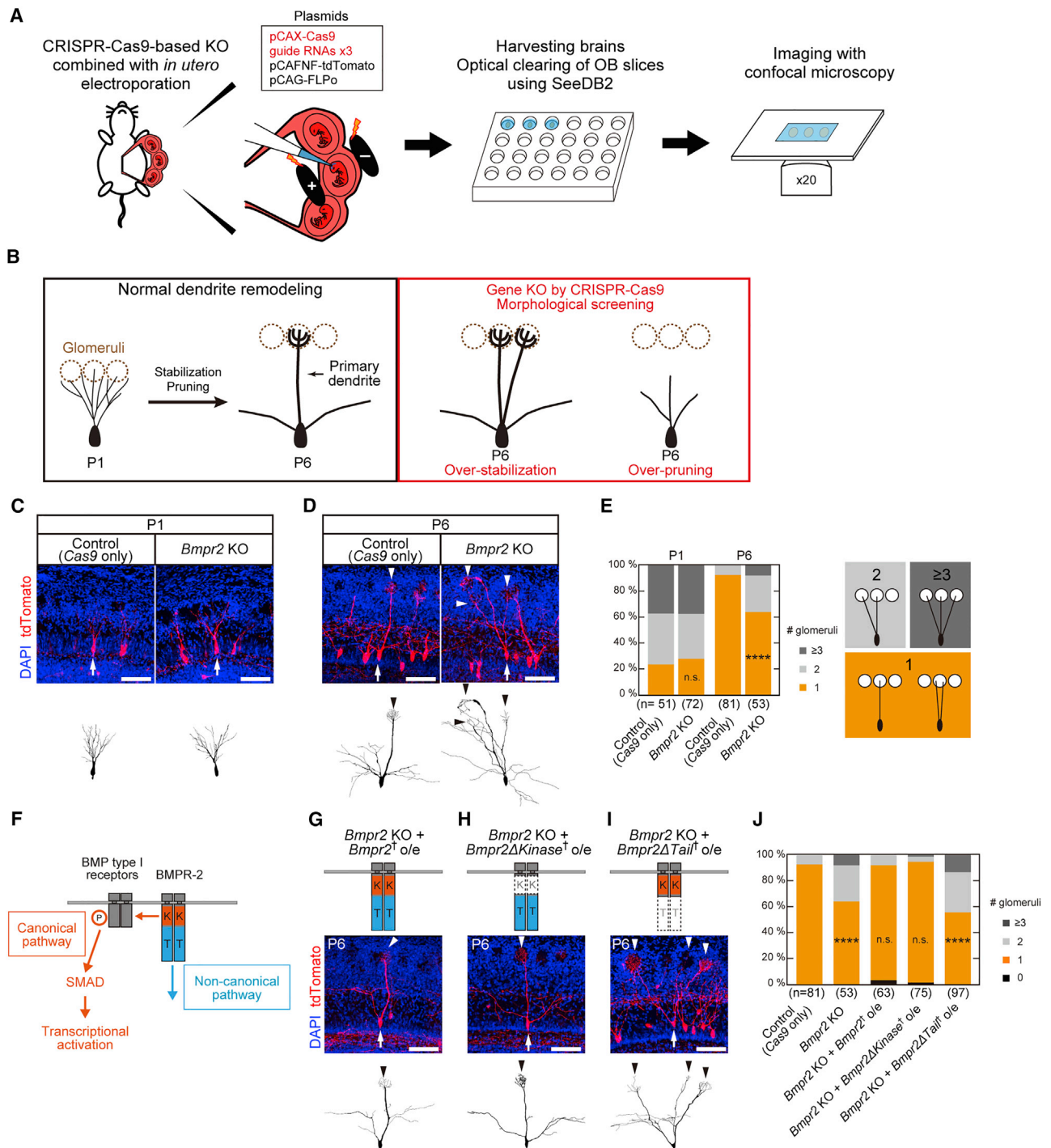


**Figure 1. BMPR-2 tail domain is required for dendrite destabilization in mitral cells**

(A) Schema showing CRISPR-Cas9-based KO screening.

(B) Development of mitral cells from P1 to P6. A mitral cell establishes a single primary dendrite through the dendrite stabilization and pruning processes. We screened for genes controlling dendrite remodeling based on the morphology of primary dendrites at P6.

(C and D) Representative images of control and *Bmpr2* KO mitral cells at P1 (C) and P6 (D). Arrows and arrowheads indicate somata and primary dendrites, respectively. Representative neurons are reconstructed and shown below. Scale bars, 100  $\mu$ m.

(E) Quantification of the number of glomeruli innervated per mitral cell. Approximately 5% of mitral cells extend multiple primary dendrites to the same glomerulus. This case was counted as innervating 1 glomerulus. n.s., non-significant. \*\*\*\* $p < 0.0001$  ( $\chi^2$  test, compared with the control). n, number of mitral cells.

(legend continued on next page)

## RESULTS

### Screening for cell surface receptors regulating dendrite remodeling in mitral cells

To gain insight into the mechanisms of selective dendrite remodeling, we screened for cell surface receptors that control dendritic growth and/or remodeling based on extrinsic cues. First, we obtained transcriptome data for developing mitral cells labeled by *in utero* electroporation. Single-cell cDNA was prepared from mitral cells at postnatal day (P) 3 and P6, and gene expression profiles were analyzed using a microarray (Imai et al., 2009). We focused on cell surface receptors abundantly expressed in developing mitral cells (Figure S1).

To test their functional roles in dendrite development, we performed CRISPR-Cas9-based KO screening combined with *in utero* electroporation (Figure 1A; Straub et al., 2014). To maximize the KO efficiency of any gene, we used the triple-target CRISPR method: Three guide RNAs (gRNAs) were designed per gene and introduced to neurons together (Figure S1A; Sunagawa et al., 2016). We electroporated tdTomato, Cas9, and the three gRNA plasmids into mitral cell progenitors at embryonic day (E) 12 to label and manipulate gene functions in mitral cells. Mitral cells are generated between E10 and E12 and are potentially heterogeneous in terms of maturation timing (Hirata et al., 2019; Imamura et al., 2011); however, the mechanisms of dendrite remodeling seem to be shared (Fujimoto et al., 2019). It is unrealistic to examine the KO efficiency for all genes because antibodies are not available for all of them. However, control experiments with two representative genes, *Eomes* (*Tbr2*) and *Tbx21*, demonstrated a highly efficient KO ratio with this strategy. On average, 71% of tdTomato-positive mitral cells lacked protein expression (Figures S1B–S1E). We therefore performed *in vivo* KO screening for the candidate genes (some were double or triple KO during the initial round of screening). OB samples were collected at P1 and/or P6, and dendrite morphology of mitral cells was comprehensively analyzed via tissue clearing, SeeDB2, and volumetric imaging (Figures 1A and 1B). Among the 38 genes tested, *Bmpr2* demonstrated the most prominent defects in dendrite development (Figures S1F and S1G). When analyzed at P6, 93% of wild-type mitral cells formed single primary dendrites. However, only 64% of mitral cells formed a single primary dendrite when *Bmpr2* was knocked out; the remaining neurons retained connections to multiple glomeruli (Figures 1D and S2A). The total volume of the dendritic tuft also increased in *Bmpr2* KO mitral cells (Figures S2F–S2M). In contrast, the formation of lateral dendrites was not affected (Figures S2D and S2E). We did not find obvious differences between control and *Bmpr2* KO at P1, excluding a role for *Bmpr2* during the initial dendritic outgrowth (Figure 1C). Thus, *Bmpr2* is either directly or indirectly involved in the pruning of primary dendrites that occurs during the remodeling process.

### The BMPR-2 tail domain is required for normal dendrite remodeling

BMP signaling plays important roles in various aspects of development, from embryonic body patterning to neurite and synapse formation (Bragdon et al., 2011; Dutko and Mullins, 2011). BMP receptors are composed of two types, type I and II. BMPR-2 is a member of the type II receptor group. The receptors' intracellular signals are divided into canonical and non-canonical pathways (Figure 1F). The canonical pathway is initiated by the phosphorylation of the type I receptor by the kinase domain of the type II receptor, leading to transcriptional activation through SMAD proteins. The non-canonical pathway is mostly mediated by the C-terminal tail domain of BMPR-2 receptors (Fioletta et al., 2003). To determine which pathway is required for normal dendrite remodeling in mitral cells, we performed *Bmpr2* KO rescue experiments using BMPR-2 deletion mutants.

When a gRNA-resistant full-length BMPR-2 was co-expressed, the defective dendrite remodeling by *Bmpr2* KO was fully rescued (a single primary dendrite was formed in 92% of mitral cells) (Figure 1G), excluding the possibility of an off-target effect of the CRISPR-Cas9 KO. Next, we expressed a kinase domain-deleted BMPR-2 mutant (*Bmpr2 $\Delta$ Kinase*) combined with the *Bmpr2* KO. In this situation, mitral cells cannot mediate the canonical pathway via BMPR-2. Mitral cells still formed single primary dendrites (single: 95%) (Figure 1H), suggesting that the canonical pathway is not needed for normal dendrite remodeling. However, a rescue experiment with a tail domain-deleted BMPR-2 mutant (*Bmpr2 $\Delta$ Tail*) failed to rescue the KO phenotype (single: 56%), suggesting that the non-canonical pathway through the BMPR-2 tail domain is involved in the dendrite remodeling (Figure 1I).

We also examined whether ligand binding to the BMPR-2 is required to ensure single primary dendrites. When an extracellular (EC) domain-deleted BMPR-2 mutant (*Bmpr2 $\Delta$ EC*) was expressed combined with the *Bmpr2* KO, single primary dendrites were still formed (single: 83%) (Figures 2A and 2B). This result indicates that BMPR-2 permits normal dendrite pruning without ligand binding (Figure 2C).

### The BMPR-2 tail domain inhibits LIMK1 to facilitate dendrite destabilization

The targets for non-canonical BMP pathways include LIMK, p38/mitogen-activated protein kinase (MAPK), phosphatidylinositol 3-kinase (PI3K), and Cdc42 (Gámez et al., 2013). Earlier studies have shown that BMPR-2 regulates neurite extension via LIMK (Fioletta et al., 2003; Lee-Hoeflich et al., 2004; Wen et al., 2007). The BMPR-2 tail domain was reported to capture the LIM domain of LIMK, which is required for interaction with its activators, such as Rock and PAK (Fioletta et al., 2003). It is also known that active LIMK inhibits an actin depolymerization protein, cofilin, by phosphorylation, thereby stabilizing F-actin (Zebda et al., 2000). Therefore, we examined whether dendritic

(F) Schematic representation of the two BMP signaling pathways. The canonical pathway is mediated by a kinase domain of BMPR-2, BMP type I receptors, and SMADs, leading to transcriptional activation. The non-canonical pathway is mediated by the C-terminal tail domain of BMPR-2. K, kinase domain; T, tail domain. (G–I) Rescue of *Bmpr2* KO phenotype with deletion mutants of *Bmpr2*. Guide RNA-resistant *Bmpr2* was used for the rescue experiments. † indicates a guide RNA-resistant *Bmpr2*. o/e, overexpression. Age, P6. Scale bars, 100  $\mu$ m.

(J) Number of glomeruli innervated per mitral cell was quantified. \*\*\*\*p < 0.0001 ( $\chi^2$  test with Bonferroni correction, compared with the control).

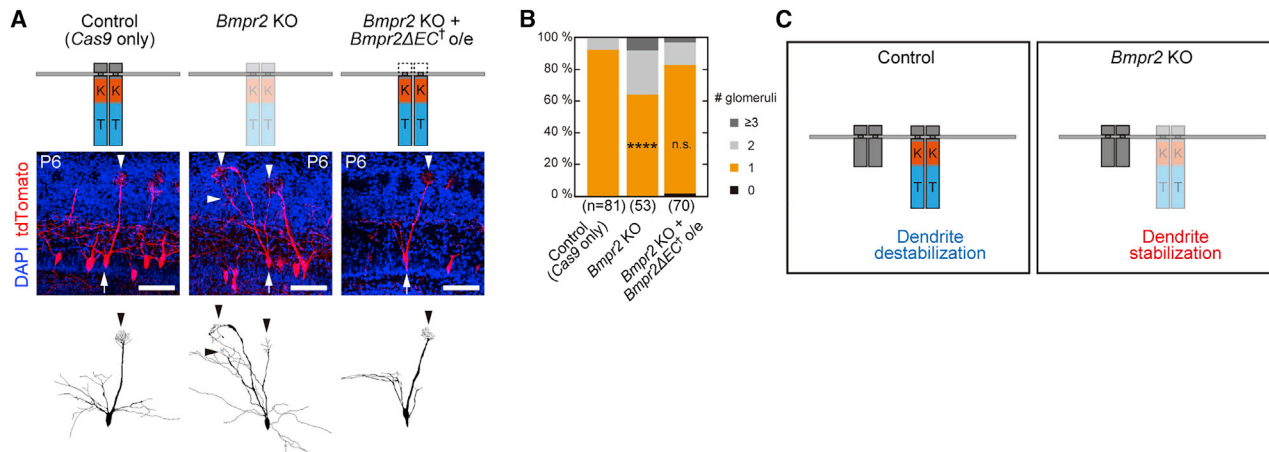


**Figure 2. BMPR-2 facilitates dendrite destabilization without BMP ligands**

(A) Rescue of *Bmpr2* KO using *Bmpr2ΔEC*, which lacks the extracellular domain. Control and *Bmpr2* KO images are the same as in Figure 1D. *o/e*, over-expression. Age, P6. Scale bars, 100  $\mu$ m.  
 (B) Quantification of the number of glomeruli innervated by single mitral cells. \*\*\*\* $p < 0.0001$  ( $\chi^2$  test with Bonferroni correction, compared with the control).  
 (C) Schema illustrating the role of BMPR-2 in dendrite destabilization. A BMPR-2 C-terminal tail facilitates dendrite destabilization without BMP ligands.

stability is controlled by BMPR-2-LIMK interaction during the developmental remodeling process.

We overexpressed one of the LIMKs, LIMK1, in mitral cells. We found that multiple primary dendrites are formed when LIMK1 was overexpressed, similar to the *Bmpr2* KO phenotype (single: 58%) (Figures 3A and 3B). Because LIMK is known to promote F-actin formation (Zebda et al., 2000), the formation of multiple primary dendrites likely results from the overstabilization of F-actin. We also found that the LIMK1 overexpression phenotype is rescued by the overexpression of BMPR-2 (single: 84%), supporting the notion that BMPR-2 inhibits LIMK1 in mitral cells (Figure 3C). Rescue experiments with a series of deletion mutants (*Bmpr2ΔKinase*, *Bmpr2ΔTail*, and *Bmpr2ΔEC*) revealed that the BMPR-2 tail domain inhibits LIMK1 without the presence of BMP ligands (single: 89%, 62%, and 77%, respectively) (Figures 3D–3G). These results suggest that ligand-free BMPR-2 inhibits LIMK, thereby preventing excessive stabilization of F-actin and dendrites (Figure 3H).

### BMP ligands promote dendrite stabilization

We next examined the role of BMP ligands in dendrite remodeling. To inhibit ligand binding to all BMPRs in mitral cells, we expressed a BMP antagonist, Noggin, in mitral cells (Groppe et al., 2002; Zimmerman et al., 1996). Although most mitral cells formed a single primary dendrite, 8 of 122 mitral cells (6.6%) failed to extend primary dendrites into the glomerular layer (Figures 4A and 4B). We did not find this phenotype in controls. This suggests that ligand binding to BMPRs facilitates the formation of mature primary dendrites.

BMPs are members of the transforming growth factor (TGF)  $\beta$  superfamily. It has been known that BMPR-2 can potentially bind to 13 types of ligands (Mueller and Nickel, 2012). Therefore, we examined the expression of all 13 types by qPCR and found that BMP2, BMP4–BMP8, BMP10, BMP15, GDF2, GDF5–GDF7, and GDF9 are expressed in the olfactory epithelium (OE) and/or OB at P3 and P6 (Figure 4C; Peretto et al., 2002).

We then overexpressed each of these ligands in mitral cells using *in utero* electroporation, expecting autocrine and/or paracrine effects. We could not obtain BMP10 and GDF2 samples, because overexpression of these ligands impaired brain development (data not shown). Among the remaining BMPs and GDFs, only BMP2 and BMP4 affected dendrite remodeling (Figures 4D and 4E): More primary dendrites were formed by BMP2 and BMP4 overexpression (single: 51% and 53%, respectively). These results indicate that BMPR-2 destabilizes dendrites through LIMK inhibition without ligands but stabilizes dendrites upon ligand binding, most likely by releasing LIMK from its tail domain (Figure 4G; Foletta et al., 2003).

*In situ* hybridization of *Bmp2* and *Bmp4* mRNA revealed its localization at the surface of the OB, but not the OE (Figures S3A–S3D). Immunostaining for a meningeal marker, ER-TR7, revealed that *Bmp4* is expressed in meninges (Figure 4F). *Bmp2* showed a pattern similar to that of *Bmp4* but at a lower level. To examine the protein localization of BMP4, we generated *GFP::Bmp4* knockin mice; however, we could not reliably detect the GFP signals because of technical limitations (data not shown). In general, it is extremely difficult to immunostain secreted guidance molecules. Although we cannot know the localization of secreted BMP proteins, the mRNA data suggest that BMP is enriched in the surface of the OB.

### Rac1 and PAK activate LIMK1 to stabilize dendrites

How then is the free LIMK activated to stabilize dendrites? It is known that the phosphorylation of LIMK is induced by Rho-family small guanosine triphosphatases (GTPases), such as RhoA, Cdc42, and Rac1 (Jaffe and Hall, 2005). We overexpressed these small GTPases in mitral cells and found that only Rac1 overexpression leads to multiple primary dendrites at P6 (single: 90%, 90%, and 45%, respectively) (Figures 5A–5D). Moreover, this phenotype was rescued when combined with a *Limk1* KO (single: 83%), suggesting that Rac1 stabilizes dendrites through LIMK1 (Figure 5E). We also tested PAK, an immediate

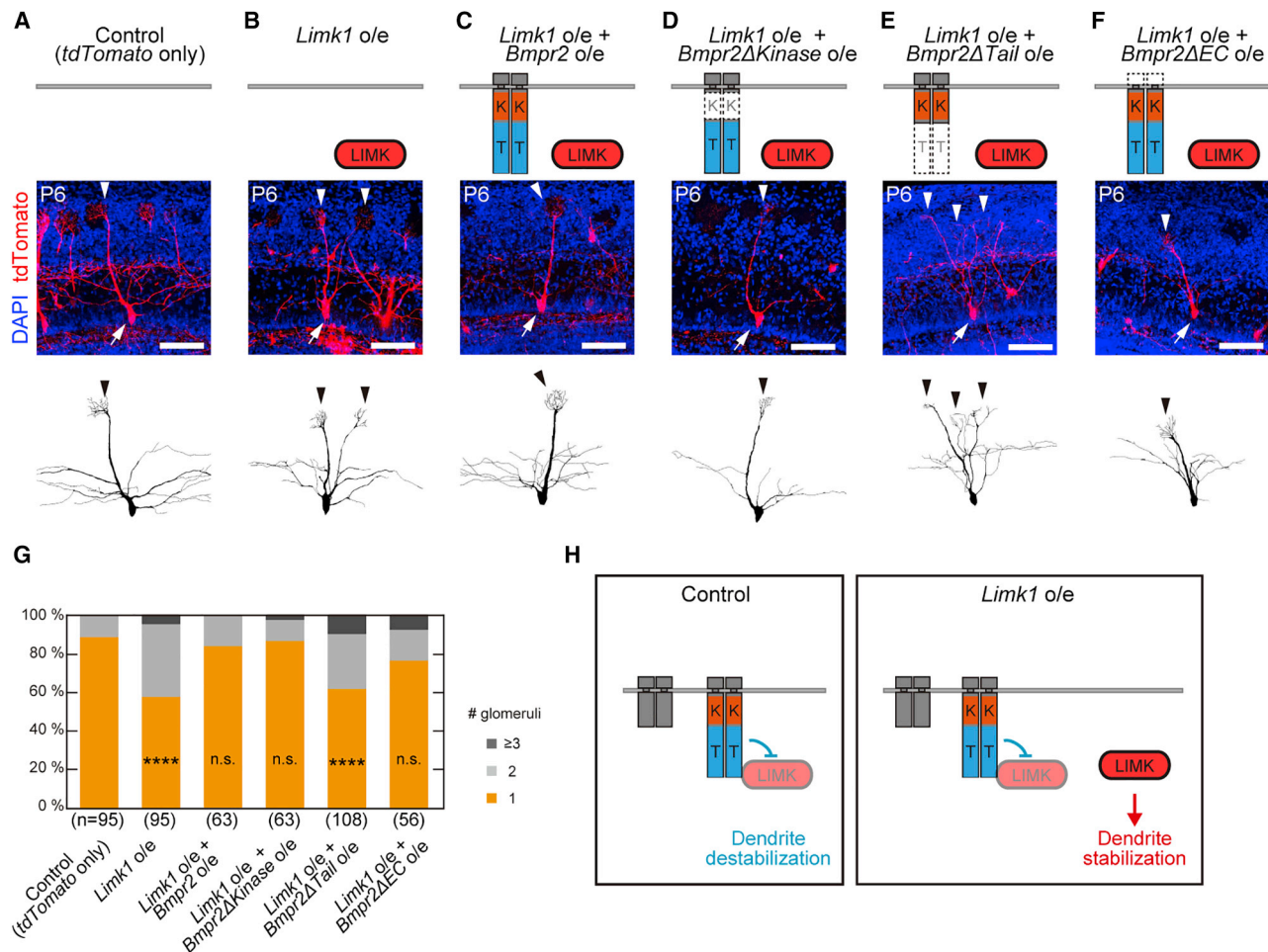


**Figure 3. BMPR-2 tail domain inhibits LIMK1 and thereby facilitates dendrite destabilization**

(A–F) Overexpression of *Limk1* and its rescue by *Bmpr2* deletion mutants. *Limk1* overexpression (*o/e*) leads to the formation of multiple primary dendrites. This phenotype was suppressed by the C-terminal tail domain of BMPR-2. Age, P6. Arrows and arrowheads indicate somata and primary dendrites, respectively. Scale bars, 100  $\mu$ m.

(G) Quantification of the number of glomeruli innervated per cell in (A)–(F). \*\*\*\* $p < 0.0001$  ( $\chi^2$  test with Bonferroni correction, compared with the control).

(H) Schematic summary of the results. *Limk1* overexpression leads to the formation of multiple primary dendrites in mitral cells. However, the C-terminal tail domain of BMPR-2 rescued this phenotype without ligand when overexpressed.

downstream target of Rac1. Overexpression of *Pak1* showed a similar phenotype to the *Rac1* overexpression, forming multiple primary dendrites (single: 41%) (Figure 5F).

Next, we examined the interplay between BMPR-2 and Rac1 in dendrite remodeling. Although the overexpression of Rac1 resulted in multiple primary dendrites, the overexpression of BMPR-2 rescued this phenotype (single: 85%) (Figure 5G). These results suggest that BMPR-2 has a gating function for Rac1 signaling: Rac1 signals are conveyed to LIMK and facilitate dendrite stabilization only when the BMP ligands bind to BMPR-2 (Figure 5I).

### Glutamatergic inputs via NMDARs activate Rac1 at dendritic tufts

Rac1 is known to play a key role in long-term potentiation based on glutamatergic synaptic inputs via NMDARs in hippocampal

neurons (Nakahata and Yasuda, 2018; Tu et al., 2020). Therefore, we considered the possibility that Rac1 is activated by neuronal activity in developing mitral cells. We introduced a Förster resonance energy transfer (FRET) biosensor for Rac1, RaichuEV-Rac1 (Komatsu et al., 2011), into mitral cells using *in utero* electroporation. We prepared OB slices from P3–P5 mice, and FRET signals were monitored with 2-photon microscopy (Figure 6A).

In the control experiment, we used *Thy1-GCaMP6f* transgenic mice, in which GCaMP6f was specifically expressed in mitral/tufted cells. NMDA application (100  $\mu$ M) produced robust  $Ca^{2+}$  responses both in mitral cell somata and in dendritic tufts (Figures 6B and 6D). In FRET imaging for Rac1, NMDA application also produced robust responses in mitral cells (Figures 6C and 6E). The NMDAR antagonist AP5 (100  $\mu$ M) abolished the FRET responses to NMDA. We also confirmed that a mutant

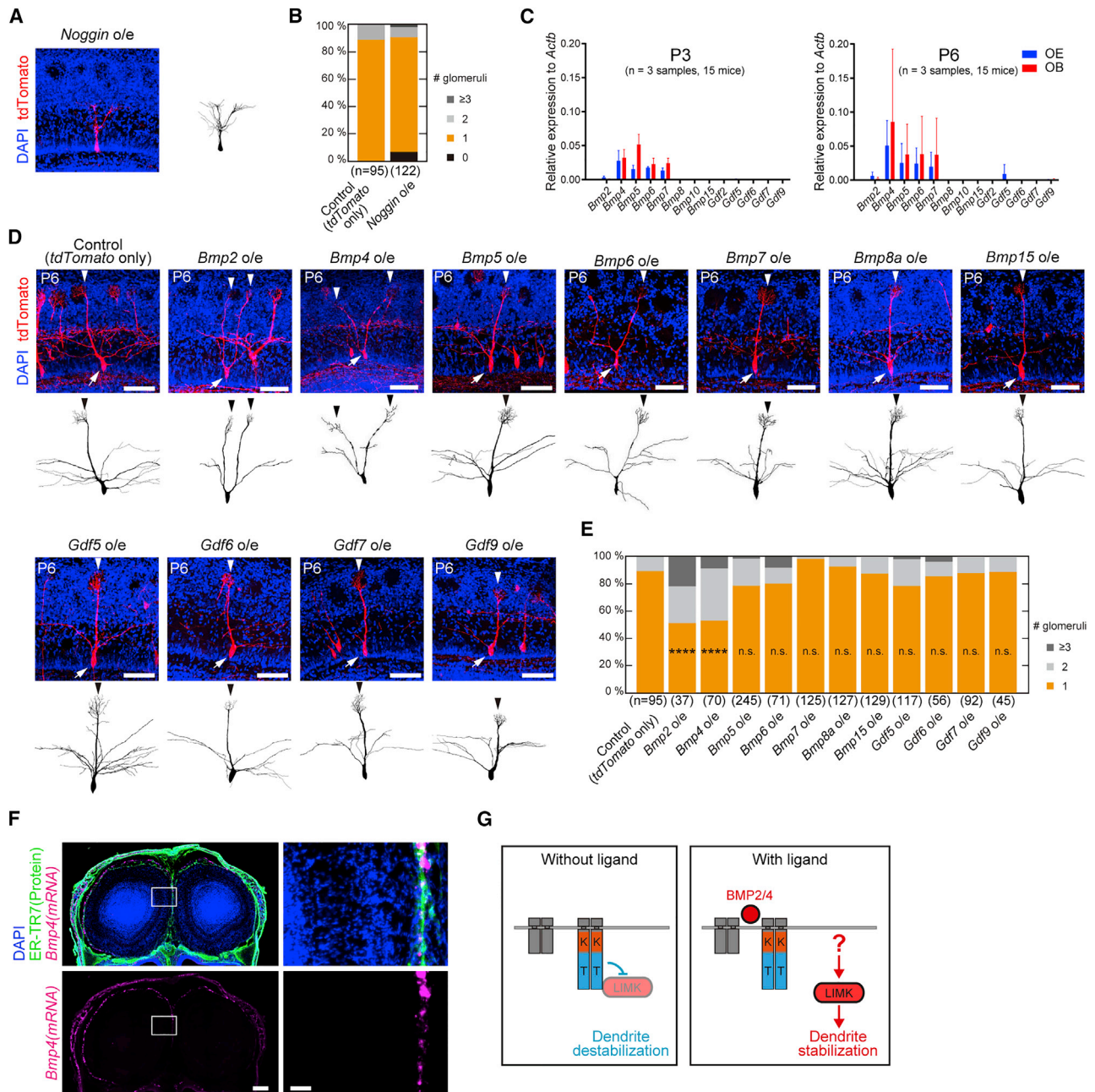


**Figure 4. BMP2/4 stabilize dendrites**

(A) Overexpression (o/e) of the BMP antagonist, Noggin. Some mitral cells did not have primary dendrites. See also Figure S3G, excluding a contribution of apoptosis. Age, P6. Arrows and arrowheads indicate somata and primary dendrites, respectively. Scale bars, 100  $\mu$ m.

(B) Quantification of the number of glomeruli innervated per mitral cell.

(C) Expression of BMP ligand genes in the OE and OB at P3 and P6. The expression levels were determined by qPCR and normalized to the *Actb* expression levels. Each cDNA pool was synthesized from mRNAs collected from 5 mice. Error bars represent SD.

(D) Overexpression of BMP and GDF genes in mitral cells. The control image is the same as in Figure 3A. Age, P6. Scale bars, 100  $\mu$ m.

(E) Quantification of the number of glomeruli innervated per mitral cell. \*\*\*\*p < 0.0001 ( $\chi^2$  test with Bonferroni correction, compared with the control).

(F) Localization of *Bmp4* mRNA was analyzed by *in situ* hybridization (RNA scope) combined with immunostaining for a meninge marker, anti-ER-TR7 immunostaining. Scale bars, 250  $\mu$ m (left) and 100  $\mu$ m (right).

(G) Schematic summary of the experiment. Ligand-free BMPR-2 facilitates dendrite destabilization by inhibiting LIMK. However, when bound to BMP2/4, BMPR-2 facilitates dendrite stabilization, most likely by releasing LIMK.

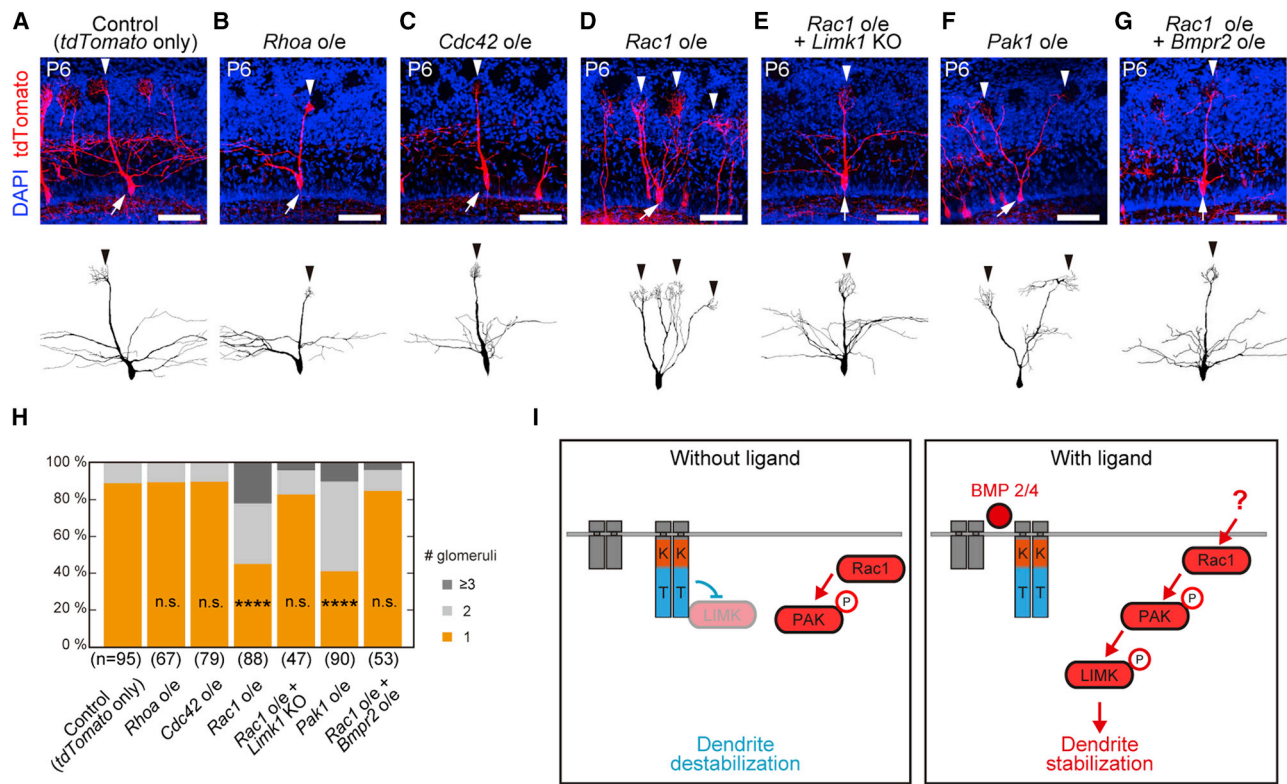


**Figure 5. Free LIMK1 is activated by Rac1 through PAK**

(A–G) Overexpression (o/e) of the Rho-family small GTPases. Overexpression of *Rac1*, but not *Rhoa* and *Cdc42*, led to multiple primary dendrites. The phenotype of *Rac1* overexpression was rescued by *Limk1* KO or *Bmpr2* overexpression. The control image is the same as in Figure 3A. Age, P6. Arrows and arrowheads indicate somata and primary dendrites, respectively. Scale bars, 100  $\mu$ m.

(H) Quantification of the number of glomeruli innervated per mitral cell. \*\*\*\* $p < 0.0001$  ( $\chi^2$  test with Bonferroni correction, versus control).

(I) Schematic summary of experiments showing the activation mechanisms of LIMK. The BMP2/4-bound BMPR-2 likely releases LIMK. The free LIMK is activated by Rac1 and PAK, leading to the stabilization of primary dendrites.

RaichuEV-Rac1 (T17N), which contains the inactive form of the Rac1 domain, did not produce FRET responses. Rac1 FRET signals were more prominent in dendritic tufts than in somata, which was not seen for GCaMP6f  $Ca^{2+}$  imaging (Figure 6E). These results demonstrate that glutamatergic inputs through NMDARs induce Rac1 activation in developing mitral cells, especially in dendritic tufts.

We examined how Rac1 is activated within mitral cells. We examined the responses of mitral cells to NMDA (100  $\mu$ M) and AMPA (100  $\mu$ M) in the presence of the sodium channel blocker tetrodotoxin (TTX). In the control experiments with GCaMP6f,  $Ca^{2+}$  responses to NMDA and AMPA were comparable (Figure 6F). In contrast, the FRET signals for Rac1 showed stronger responses to NMDA than to AMPA, indicating that an NMDAR-mediated  $Ca^{2+}$  influx, rather than voltage-gated  $Ca^{2+}$  channels, is the major source of Rac1 activation (Figure 6G).

### F-actin formation occurs preferentially at dendritic tufts

How can activated LIMK stabilize dendrites? LIMK is known to phosphorylate cofilin at S3 (Oser and Condeelis, 2009). Although non-phosphorylated cofilin facilitates F-actin severing and disassembly, phosphorylated cofilin allows F-actin formation (Bernstein and Bamberg, 2010). Therefore, we tested whether

cofilin controls F-actin stability and dendritic remodeling downstream of LIMK in mitral cells. When an active form cofilin mutant (phosphoblock S3A substitution, cofilin1(S3A) hereafter) was introduced by *in utero* electroporation and expressed under the CAG promoter, neuronal migration was impaired (Figure S4A). We, therefore, expressed cofilin1(S3A) from P0 using the Tet-On system and doxycycline administration (P0–P6). When *Limk1* alone was overexpressed, multiple primary dendrites were formed at P6; however, the expression of *cofilin1(S3A)* from P0 rescued the *Limk1* overexpression phenotype, forming single primary dendrites (single: 58% and 85%, respectively) (Figures 7A and 7B). This result indicates that LIMK stabilizes dendrites by phosphorylating cofilin.

Because LIMK stabilizes dendrites through cofilin phosphorylation, we assumed that cofilin phosphatases may play an opposing role in dendrite remodeling. Here we examined the role of Slingshot, which is known to dephosphorylate cofilin (Niwa et al., 2002). We performed a triple KO of *Slingshot* genes (*Slingshot1*, *Slingshot2*, and *Slingshot3*) using the CRISPR-Cas9 system combined with *in utero* electroporation. The *Slingshot* triple KO demonstrated impairment in dendrite pruning (single: 70%) (Figures 7C and 7D). In contrast, *Slingshot1* overexpression caused loss of primary dendrites in 2 of 90 mitral cells

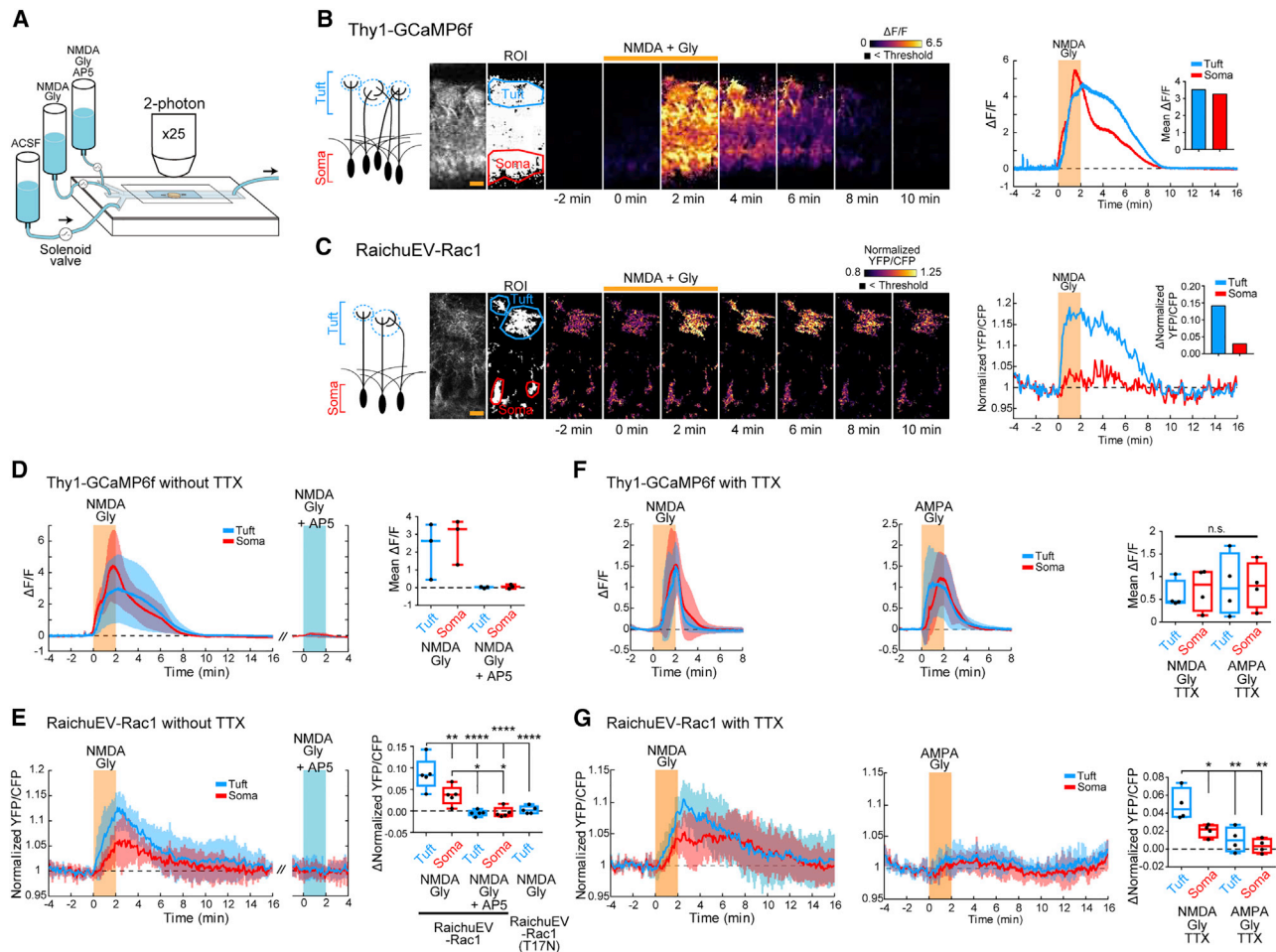


**Figure 6. Rac1 is activated by neuronal activity via NMDAR**

(A) Schematic of the OB slice imaging. Acute OB slices were prepared from P3–P5 mice. Artificial corticospinal fluid (ACSF) and other drug cocktails were perfused from syringes by gravity. The flow was controlled by solenoid valves. GCaMP or FRET signals were monitored by 2-photon microscopy.

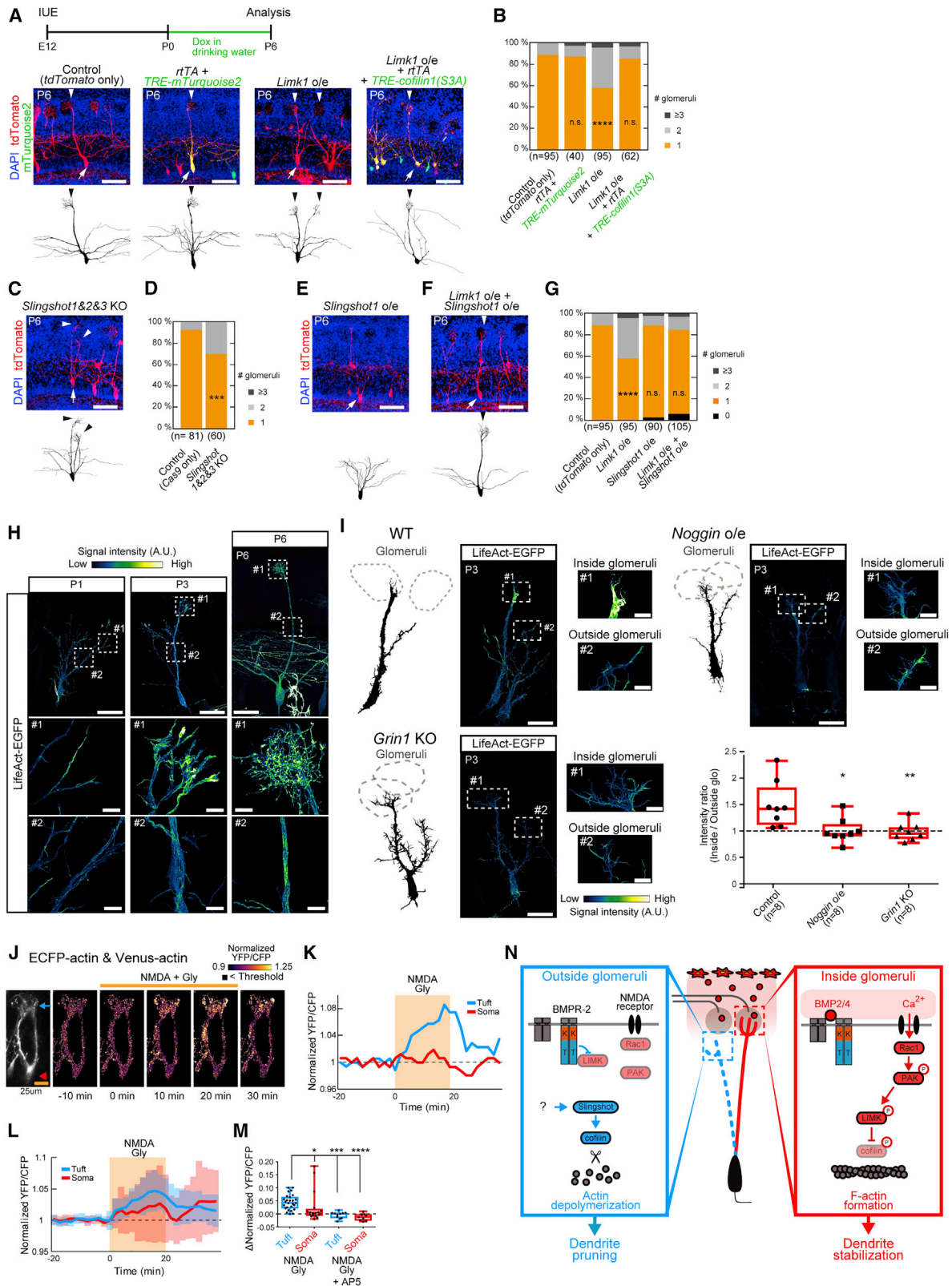
(B and C) Representative responses of Ca<sup>2+</sup> and FRET signals. For Ca<sup>2+</sup> imaging, Thy1-GCaMP6f transgenic mice were used in which mitral/tufted cells are specifically labeled. For Rac1 FRET imaging, pCAGGS-RaichuEV-Rac1 was introduced into mitral/tufted cells by *in utero* electroporation. 100  $\mu$ M NMDA and 40  $\mu$ M Gly was applied during 0–2 min. Pixels below the threshold level of basal fluorescence are shown in black. Images were processed with a median filter. GCaMP6f signals are shown as  $\Delta F/F$  values in pseudocolor. FRET signals are shown as the normalized YFP/CFP ratio. Left images show the field of view. Regions of interest (ROIs) were drawn on the tuft and soma areas, and the time courses are shown on the right. Orange shades indicate the stimulation period (2 min). Scale bars, 25  $\mu$ m.

(D and E) Average time courses of Ca<sup>2+</sup> and FRET signals at tufts (blue) and somata (red) ( $n = 3$  and 5 mice, respectively). SD is shown by pale colors behind the traces. Orange and blue shades represent the NMDA and NMDA + AP5 stimulation period, respectively. Quantification of the mean responses (0–3 min) is shown on the right. In the boxplots, whiskers represent the maximum and minimum, boxes represent the inter-quartile range, and horizontal lines represent the median. Black dots represent individual slices. Mean  $\Delta F/F$  and  $\Delta$ normalized YFP/CFP for 3 min were calculated, in which the mean signals before stimulation (1 min) were used as references. An inactive mutant of RaichuEV-Rac1 (T17N) was also tested. \*\* $p < 0.01$ , \*\*\*\* $p < 0.0001$  (one-way ANOVA with Tukey's post hoc test).

(F and G) Average time courses of Ca<sup>2+</sup> and FRET signals under TTX ( $n = 4$  mice each). Orange shades represent the NMDA or AMPA + Gly stimulation period. Quantification of the responses is shown on the right. \* $p < 0.05$ , \*\* $p < 0.01$  (one-way ANOVA with Tukey's post hoc test).

(Figures 7E and 7G), supporting the notion that Slingshot facilitates dendrite pruning. We also found that the *Limk1* overexpression phenotype is rescued by the co-expression of *Slingshot1* (single: *Limk1* 58%, *Limk1* + *Slingshot1* 84%, and 6/105 cells had no primary dendrite) (Figures 7F and 7G). These results indicate that cofilin plays a pivotal role in dendrite remodeling: Phosphorylation and dephosphorylation of cofilin lead to stabilization and destabilization of primary dendrites, respectively.

Next, we examined whether F-actin formation and disassembly are spatially controlled during the dendrite remodeling process. To visualize F-actin formation, we expressed an F-actin marker, LifeAct-EGFP in mitral cells. The LifeAct signal was most prominent at the dendritic tips early in development (P1–P3), but it gradually spread to the dendritic shafts and somata at later stages (Figures 7H, S4B, and S4C). We next examined whether LifeAct signals are different in different dendrites during the



(legend on next page)

remodeling process. We found that LifeAct signals are stronger at the dendritic tips extending into the glomerular layer than those retained in the external plexiform layer (Figures 7I and S5). Moreover, this biased localization of LifeAct signals was lost in *Noggin*-overexpressed and *Grin1* KO mitral cells (Figures 7I and S5). These results suggest that BMP signaling and NMDAR activation in glomeruli promote localized F-actin formation and dendritic stabilization.

We also evaluated the formation of excitatory synapses (post-synaptic density [PSD]) in mitral cells using a PSD95 deletion mutant fused to EGFP (PSD $\Delta$ 1.2-EGFP) (Figures S2F–S2H; Hayashi-Takagi et al., 2015). The dendritic tuft volume and the number of PSDs were increased in *Bmpr2* KO, suggesting that BMPR-2 suppresses synapse formation too (Figures S2F–S2M); we assume that this is because a significant fraction of BMPR-2 is free of ligands even within glomeruli. However, both the size and the number of PSDs were reduced in *Grin1* KO mitral cells. Thus, NMDAR signals facilitate the formation of stable excitatory synapses.

So far, we have demonstrated that both NMDARs and BMP signaling are required to accumulate F-actin in dendritic tips within glomeruli. To directly observe F-actin formation in dendrites within glomeruli, we performed FRET imaging for actin polymerization in acute OB slices at P3–P5. Here, we introduced ECFP-fused actin and Venus-fused actin in mitral cells (Okamoto et al., 2004). We found that FRET signals were increased upon NMDA application, suggesting F-actin forma-

tion (Figures 7J–7M). FRET signals were increased in the dendritic tufts within glomeruli, but rarely in somata. Thus, F-actin formation and dendrite stabilization occur exclusively within glomeruli.

## DISCUSSION

### Gating function of BMPR-2 and positive feedback regulation in dendrite stabilization

In this study, we revealed the bidirectional role of BMPR-2 in dendrite remodeling: Ligand-free BMPR-2 permits dendrite destabilization, whereas ligand-bound BMPR-2 promotes dendrite stabilization. These functions are mediated by the intracellular tail domain of BMPR-2, which inhibits LIMK activity in the absence of ligand and releases it upon ligand binding. However, ligand binding alone does not induce dendrite stabilization. The released LIMK has to be activated by neuronal activity through the NMDAR-Rac1-PAK pathway to stabilize dendrites. Activated LIMK phosphorylates cofilin and thereby facilitates F-actin formation at the dendritic tufts, thus leading to dendrite stabilization. Therefore, dendrites are stabilized only when BMP ligands and glutamatergic inputs co-exist (Figure 7N).

Unfortunately, we were unable to directly localize BMP ligands or activation of BMPR-2 due to technical limitations. However, because BMP2 and BMP4 are secreted from the OB surface, we assume that BMP concentrations are higher at the surface of the OB. Possibly, the extracellular matrix may help localize

### Figure 7. Regulation of the actin cytoskeleton by cofilin at tufts is key for dendrite remodeling

(A) Phosphoblocked cofilin1 mutant, cofilin1(S3A), rescued the phenotype of *Limk1* overexpression (o/e). In this experiment, *cofilin1*(S3A) was expressed using the Tet-On system (*rtTA* and *TRE-cofilin1*(S3A)), because *cofilin1*(S3A) was found to affect neuronal migration at an earlier stage. *cofilin1*(S3A) expression was induced by doxycycline (2 mg/mL) in drinking water from P0. The control and *Limk1* o/e images are the same as in Figures 3A and 3B. Age, P6. Arrows and arrowheads indicate somata and primary dendrites, respectively. Scale bars, 100  $\mu$ m.

(B) Quantification of the number of glomeruli innervated by single mitral cells. \*\*\*\* $p < 0.0001$  ( $\chi^2$  test with Bonferroni correction, versus control).

(C) Slingshot triple KO (*Slingshot1*, *Slingshot2*, and *Slingshot3*) using the CRISPR-Cas9 system combined with *in utero* electroporation. Age, P6. Scale bars, 100  $\mu$ m.

(D) Quantification of the number of glomeruli innervated per mitral cell. \*\*\* $p < 0.001$  ( $\chi^2$  test, versus control).

(E and F) Overexpression of *Slingshot1* (E). The phenotype of *Limk1* overexpression was rescued by co-overexpression of *Slingshot1* (F). Age, P6. Scale bars, 100  $\mu$ m.

(G) Quantification of the number of glomeruli innervated per mitral cell. Mitral cells with no primary dendrites were excluded from the statistical tests. \*\*\*\* $p < 0.0001$  ( $\chi^2$  test, with Bonferroni correction, versus control).

(H) Visualization of F-actin with LifeAct-EGFP at different stages of dendrite remodeling. Top panels show low-magnification images. Middle and bottom images show high-magnification images of dendritic tufts and shafts, respectively. Scale bars, 50  $\mu$ m (top) and 10  $\mu$ m (middle and bottom).

(I) Representative mitral cell extending dendrites to both inside and outside glomeruli. Traces are shown on the left. Quantification of LifeAct-EGFP signals in primary dendrites inside and outside glomeruli are shown in the graph. The average intensity within 30  $\mu$ m of the tip of the dendrites was analyzed. In the boxplots, whiskers represent the maximum and minimum, boxes represent the inter-quartile range, and horizontal lines represent the median. Black dots represent individual mitral cells. Additional raw images are shown in Figure S5. Age, P3. Scale bars, 50  $\mu$ m (left) and 10  $\mu$ m (right). \* $p < 0.05$ , \*\* $p < 0.01$  (one-way ANOVA with Tukey's post hoc test).

(J) Representative data of actin FRET imaging in mitral cells. We applied 30  $\mu$ M NMDA and 12  $\mu$ M Gly. Changes in FRET signals are shown by pseudocolor (see color legend). A blue arrow and a red arrowhead indicate a dendritic tuft and a soma, respectively. Age, P4. Scale bar, 25  $\mu$ m.

(K) Time courses of actin FRET signals at the dendritic tuft (blue) and soma (red) shown in (J). The orange rectangle represents the duration of 30  $\mu$ M NMDA and 12  $\mu$ M Gly application.

(L and M) Average time courses for actin FRET signals at dendritic tufts (blue) and somata (red). SD is shown by pale colors behind the traces. An orange shade represents the NMDA stimulation period. Quantification of the mean responses (14–18 min) is shown in (M). Mean  $\Delta$ normalized YFP/CFP were calculated, in which the mean signals before stimulation (from –20 to 0 min) were subtracted from the response period. Age, P3–P5.  $n = 13$  mice, 16 whole cells (dendritic tufts and somata) plus 10 dendritic tufts and 2 somata for NMDA + Gly stimulation.  $n = 4$  mice, 8 whole cells plus 2 tufts and 1 soma for NMDA + Gly + AP5 stimulation. \* $p < 0.05$ , \*\*\* $p < 0.001$ , \*\*\*\* $p < 0.0001$  (Kruskal-Wallis test with Dunn's multiple comparison test).

(N) Proposed model of dendrite remodeling in mitral cells. Ligand-free BMPR-2 inhibits LIMK via its tail domain. In this situation, cofilin is dephosphorylated by Slingshot and depolymerizes actin, leading to dendrite pruning. However, BMPR-2 releases LIMK1 upon BMP2/4 binding. The free LIMK is activated by neuronal activity via NMDAR-Rac1-PAK signaling and inhibits cofilin, leading to dendrite stabilization through F-actin formation. Thus, primary dendrites can be stabilized when BMP2/4 and glutamatergic inputs co-exist. Because the BMP ligands are likely to be enriched on the OB surface, dendrites reaching the glomerular layer can be stabilized.

these proteins. However, glutamatergic inputs should occur mostly within the glomeruli. FRET imaging for Rac1 activity indicated that the NMDAR-dependent activation of Rac1 occurs preferentially in dendritic tufts within glomeruli (Figure 6C). It has been known that OSN-derived activity is dispensable for mitral cell development (Lin et al., 2000; Ma et al., 2014); however, a recent study showed that spontaneous neuronal activity is generated during the dendrite remodeling process (Fujimoto et al., 2019). We thus propose that dendrites extending to glomeruli can be selectively stabilized, whereas other dendrites that do not reach the glomerular layer are destabilized (Figure 7N). Distribution of LifeAct signals and actin FRET signals supports this idea (Figures 7, S4, and S5). Similar kinds of interplay between molecular cues and activity must be important to limit activity-dependent remodeling and plasticity to specific compartments of neurons in the nervous system.

In this study, we also found that BMP signals and NMDARs facilitate excitatory synapse maturation (Figures S2F–S2M). Because the stabilization signals are located within glomeruli, we propose that a positive feedback loop helps to stabilize one primary dendrite connecting to a glomerulus. In short, dendrites with rich glutamatergic inputs (and BMP) get richer. A similar positive feedback loop is known for axonal specification (Schelski and Bradke, 2017).

### Regulation of actin cytoskeleton in dendrite remodeling

Previous studies reported that non-canonical BMPR-2 signaling via LIMK regulates dendrite extension and arborization through ligand binding (Lee-Hoeflich et al., 2004; Saxena et al., 2018). However, our current study demonstrated that BMPR-2 has bidirectional roles in dendrite remodeling: The ligand-free BMPR-2 induces dendrite destabilization, and the ligand-bound BMPR-2 facilitates dendrite stabilization. Thus, BMPR-2 functions as a gatekeeper for dendrite stabilization signals triggered by neuronal activity in a ligand-dependent manner. Similar kinds of regulation may underlie the spine morphogenesis of cortical neurons by BMPR-2, which is considered to be affected in fragile X syndrome (Kashima et al., 2016).

There have been conflicting results regarding the roles of BMPR-2-LIMK1 interaction. One study showed that BMPR-2 inhibits LIMK1 activity, whereas another study demonstrated that BMPR-2 facilitates LIMK1 activation via Cdc42 (Foletta et al., 2003; Lee-Hoeflich et al., 2004). They performed similar *in vitro* kinase assays for LIMK1 using cofilin as a substrate, but the former used full-length BMPR-2, whereas the latter used part of the BMPR-2 tail domain. We showed that full-length BMPR-2 can rescue the phenotype of LIMK1 overexpression, supporting the former study. It is possible that the latter study used a truncated tail domain that had lost the ability to inhibit LIMK. In addition, the LIMK binding region (751–813 aa) identified in the latter study seems to play little role in our system *in vivo*: The C-terminal tail domain, rather than 751–813 aa, is critical for LIMK regulation (Figures S2N and S2O).

It is unclear whether LIMK1 is the only downstream effector of BMPR-2 in the dendrite remodeling process. We found that the *Limk1* KO cannot fully suppress the phenotype of BMP4 overexpression with multiple primary dendrites (Figures S3E and S3F). This suggests additional mechanisms exist for BMP-dependent

dendrite stabilization, e.g., MAPKs (Podkowa et al., 2010). It is also possible that canonical BMP signaling has a role in different aspects of dendrite remodeling and maturation.

The regulation of actin cytoskeleton has been extensively studied in growth cone extension and dendritic spine enlargement (Bosch and Hayashi, 2012; Luo, 2002). It has also been reported that F-actin regulation underlies dendrite development, such as extension and branching (Nithianandam and Chien, 2018; Tasaka et al., 2012). However, it has not been fully understood how the actin cytoskeleton is regulated during the dendrite remodeling process. In this study, we showed that the overexpression of LIMK1 causes dendrite stabilization by phosphorylating cofilin. This indicates that F-actin formation leads to dendrite stabilization. However, the severing and depolymerization of F-actin induced by a cofilin phosphatase Slingshot seem to facilitate dendrite pruning. Altogether, our results indicate that the regulation of the actin cytoskeleton plays a key role in dendrite remodeling. This is in contrast to the axon pruning process known to play a role in the remodeling of neuromuscular junction, in which the destabilization of microtubules plays a key role (Brill et al., 2016). Our finding is also different from dendrite pruning during *Drosophila* metamorphosis, in which local endocytosis at the dendritic neck plays a key role (Kanamori et al., 2015).

### Inter-neuronal and intra-neuronal competition in circuit remodeling

In the neuromuscular junction and cerebellar climbing fiber-Purkinje cell synapse, multiple axons compete toward one target. In other words, there is a competition among different axons from different neurons. Recent studies have identified positive and negative regulators of the activity-dependent remodeling of axons (Choo et al., 2017; Hashimoto et al., 2011; Kakegawa et al., 2015; Mikuni et al., 2013; Uesaka et al., 2014, 2018; Yasuda et al., 2021).

However, during mitral cell development, there is an intra-neuronal competition, in which different dendrites from the same neuron compete to one another to become a winner. In previous studies, positive and negative regulators for dendrite morphogenesis in mitral cells have been reported (Imamura and Greer, 2009; Inoue et al., 2018; Muroyama et al., 2016); however, they cannot fully explain the mechanisms of selective remodeling. In this study, we show how some dendrites are selectively stabilized when BMP ligands and neuronal activity co-exist. We also found that ligand-free BMPR-2 facilitates dendrite pruning; however, our results indicate that ligand-free BMPR-2 has a merely permissive role for dendrite pruning. We still do not know the active mechanisms for dendrite pruning. Slingshot seems to be one such molecule; however, it remains unclear how these molecules are regulated (Ohashi, 2015). Our unpublished results indicate that the dendritic pruning is also facilitated by glutamatergic inputs from dendrites (Fujimoto et al., 2019). This means that once all dendritic connections to glomeruli are lost, mitral cells can no longer prune dendrites and would instead regrow the dendrites. We speculate that this may be why at least one primary dendrite was maintained even when BMP signaling is genetically abolished (e.g., Noggin overexpression or *Bmpr2* KO + *Bmpr2ΔEC* overexpression). In addition, there seems to

be a critical period for the remodeling of primary dendrite, because mitral cells cannot reestablish strong glomerular connections after dendritic atrophy in the adult, leading to hyposmia (Murai et al., 2016). In the future, it will be important to study how pruning is actively controlled and what mediates intra-neuronal competition during the neurite remodeling process.

## STAR★METHODS

Detailed methods are provided in the online version of this paper and include the following:

- KEY RESOURCES TABLE
- RESOURCE AVAILABILITY
  - Lead contact
  - Materials availability
  - Data and code availability
- EXPERIMENTAL MODEL AND SUBJECT DETAILS
  - Mice
- METHOD DETAILS
  - CRISPR/Cas9
  - Plasmids
  - *In utero* electroporation
  - Single-cell cDNA preparation and microarray
  - Clearing with SeeDB2
  - Confocal imaging and image processing
  - Quantification of neuronal morphology
  - qPCR
  - *In situ* hybridization (RNA scope)
  - Ca<sup>2+</sup> and FRET imaging
- QUANTIFICATION AND STATISTICAL ANALYSIS

## SUPPLEMENTAL INFORMATION

Supplemental information can be found online at <https://doi.org/10.1016/j.celrep.2021.109276>.

## ACKNOWLEDGMENTS

We thank K. Svoboda (Thy1-GCaMP6f) for mice; P. Soriano (pPGKFLPobpA), F. Matsuzaki (pCAX-Cas9 and gRNA backbone vector), and K. Aoki (pCAGGS-RaichuEV-Rac1) for plasmids; Y. Tsunekawa, F. Matsuzaki, H. Inomata, S. Okabe, N. Nakagawa, H. Murakoshi, and R. Yasuda for technical advice; M. Nishihara, T. Ohmine, and The Research Support Center, Research Center for Human Disease Modeling, Kyushu University Graduate School of Medical Sciences, for technical assistance; and M.N. Leiwe for comments on the manuscript. Imaging experiments were in part supported by the RIKEN Kobe Light Microscopy Facility. Animal experiments were in part supported by the Laboratory for Animal Resources and Genetic Engineering at the RIKEN Center for Life Science Technologies. This work was supported by grants from the PRESTO and CREST (JPMJCR2021 to T.I.) programs of the Japan Science and Technology Agency (JST), JSPS KAKENHI (JP23680038, JP16H06456, JP17H06261, and JP21H00205 to T.I.; JP15K14327, JP17K14944, and JP19K06886 to S.F.; and JP18J10215 to S.A.), the Mochida Memorial Foundation for Medical and Pharmaceutical Research, the Uehara Memorial Foundation, and a RIKEN CDB intramural grant (to T.I.). S.A. was a junior research associate at RIKEN and a predoctoral research fellow of JSPS.

## AUTHOR CONTRIBUTIONS

S.A. performed most experiments. S.A. and R.S. optimized CRISPR-Cas9-based KO system combined with *in utero* electroporation. S.F. performed mi-

croarray experiments and helped with *in utero* electroporation. S.A. and S.F. performed Ca<sup>2+</sup> imaging and FRET imaging of OB slices. T.I. supervised the project. S.A. and T.I. wrote the manuscript.

## DECLARATION OF INTERESTS

The authors declare no competing interests.

Received: October 19, 2020

Revised: April 28, 2021

Accepted: May 28, 2021

Published: June 22, 2021

## REFERENCES

- Bernstein, B.W., and Bamberg, J.R. (2010). ADF/cofilin: a functional node in cell biology. *Trends Cell Biol.* 20, 187–195.
- Blanchart, A., De Carlos, J.A., and López-Mascaraque, L. (2006). Time frame of mitral cell development in the mice olfactory bulb. *J. Comp. Neurol.* 496, 529–543.
- Bosch, M., and Hayashi, Y. (2012). Structural plasticity of dendritic spines. *Curr. Opin. Neurobiol.* 22, 383–388.
- Bragdon, B., Moseychuk, O., Saldanha, S., King, D., Julian, J., and Nohe, A. (2011). Bone morphogenetic proteins: a critical review. *Cell. Signal.* 23, 609–620.
- Brill, M.S., Kleele, T., Ruschkies, L., Wang, M., Marahori, N.A., Reuter, M.S., Hausrat, T.J., Weigand, E., Fisher, M., Ahles, A., et al. (2016). Branch-Specific Microtubule Destabilization Mediates Axon Branch Loss during Neuromuscular Synapse Elimination. *Neuron* 92, 845–856.
- Choo, M., Miyazaki, T., Yamazaki, M., Kawamura, M., Nakazawa, T., Zhang, J., Tanimura, A., Uesaka, N., Watanabe, M., Sakimura, K., and Kano, M. (2017). Retrograde BDNF to TrkB signaling promotes synapse elimination in the developing cerebellum. *Nat. Commun.* 8, 195.
- Dana, H., Chen, T.W., Hu, A., Shields, B.C., Guo, C., Looger, L.L., Kim, D.S., and Svoboda, K. (2014). Thy1-GCaMP6 transgenic mice for neuronal population imaging *in vivo*. *PLoS ONE* 9, e108697.
- Dutko, J.A., and Mullins, M.C. (2011). SnapShot: BMP signaling in development. *Cell* 145, 636.
- Foletta, V.C., Lim, M.A., Soosairajah, J., Kelly, A.P., Stanley, E.G., Shannon, M., He, W., Das, S., Massague, J., and Bernard, O. (2003). Direct signaling by the BMP type II receptor via the cytoskeletal regulator LIMK1. *J. Cell Biol.* 162, 1089–1098.
- Fujimoto, S., Leiwe, M.N., Sakaguchi, R., Muroyama, Y., Kobayakawa, R., Kobayakawa, K., Saito, T., and Imai, T. (2019). Spontaneous activity generated within the olfactory bulb establishes the discrete wiring of mitral cell dendrites. *bioRxiv*, 625616.
- Gámez, B., Rodriguez-Carballo, E., and Ventura, F. (2013). BMP signaling in telencephalic neural cell specification and maturation. *Front. Cell. Neurosci.* 7, 87.
- Groppe, J., Greenwald, J., Wiater, E., Rodriguez-Leon, J., Economides, A.N., Kwiatkowski, W., Affolter, M., Vale, W.W., Izpisua Belmonte, J.C., and Choe, S. (2002). Structural basis of BMP signalling inhibition by the cystine knot protein Noggin. *Nature* 420, 636–642.
- Hashimoto, K., Tsujita, M., Miyazaki, T., Kitamura, K., Yamazaki, M., Shin, H.S., Watanabe, M., Sakimura, K., and Kano, M. (2011). Postsynaptic P/Q-type Ca<sup>2+</sup> channel in Purkinje cell mediates synaptic competition and elimination in developing cerebellum. *Proc. Natl. Acad. Sci. USA* 108, 9987–9992.
- Hayashi-Takagi, A., Yagishita, S., Nakamura, M., Shirai, F., Wu, Y.I., Loshbaugh, A.L., Kuhlman, B., Hahn, K.M., and Kasai, H. (2015). Labelling and optical erasure of synaptic memory traces in the motor cortex. *Nature* 525, 333–338.
- Hirata, T., Shioi, G., Abe, T., Kiyonari, H., Kato, S., Kobayashi, K., Mori, K., and Kawasaki, T. (2019). A Novel Birthdate-Labeling Method Reveals Segregated

- Parallel Projections of Mitral and External Tufted Cells in the Main Olfactory System. *eNeuro* 6, ENEURO.0234-19.2019.
- Imai, T. (2014). Construction of functional neuronal circuitry in the olfactory bulb. *Semin. Cell Dev. Biol.* 35, 180–188.
- Imai, T., Yamazaki, T., Kobayakawa, R., Kobayakawa, K., Abe, T., Suzuki, M., and Sakano, H. (2009). Pre-target axon sorting establishes the neural map topography. *Science* 325, 585–590.
- Imamura, F., and Greer, C.A. (2009). Dendritic branching of olfactory bulb mitral and tufted cells: regulation by TrkB. *PLoS ONE* 4, e6729.
- Imamura, F., Ayoub, A.E., Rakic, P., and Greer, C.A. (2011). Timing of neurogenesis is a determinant of olfactory circuitry. *Nat. Neurosci.* 14, 331–337.
- Inoue, N., Nishizumi, H., Narisuka, H., Kiyonari, H., and Sakano, H. (2018). *Sema7A/PlxnCI* signaling triggers activity-dependent olfactory synapse formation. *Nat. Commun.* 9, 1842.
- Iwasato, T., and Erzurumlu, R.S. (2018). Development of tactile sensory circuits in the CNS. *Curr. Opin. Neurobiol.* 53, 66–75.
- Jaffe, A.B., and Hall, A. (2005). Rho GTPases: biochemistry and biology. *Annu. Rev. Cell Dev. Biol.* 21, 247–269.
- Kakegawa, W., Mitakidis, N., Miura, E., Abe, M., Matsuda, K., Takeo, Y.H., Kohda, K., Motohashi, J., Takahashi, A., Nagao, S., et al. (2015). Anterograde *C1ql1* signaling is required in order to determine and maintain a single-winner climbing fiber in the mouse cerebellum. *Neuron* 85, 316–329.
- Kanamori, T., Yoshino, J., Yasunaga, K., Dairy, Y., and Emoto, K. (2015). Local endocytosis triggers dendritic thinning and pruning in *Drosophila* sensory neurons. *Nat. Commun.* 6, 6515.
- Kashima, R., Roy, S., Ascano, M., Martinez-Cerdeno, V., Ariza-Torres, J., Kim, S., Louie, J., Lu, Y., Leyton, P., Bloch, K.D., et al. (2016). Augmented non-canonical BMP type II receptor signaling mediates the synaptic abnormality of fragile X syndrome. *Sci. Signal.* 9, ra58.
- Ke, M.T., and Imai, T. (2018). Optical Clearing and Index Matching of Tissue Samples for High-resolution Fluorescence Imaging Using SeeDB2. *Bio-protocol* 8, e3046.
- Ke, M.T., Nakai, Y., Fujimoto, S., Takayama, R., Yoshida, S., Kitajima, T.S., Sato, M., and Imai, T. (2016). Super-Resolution Mapping of Neuronal Circuitry With an Index-Optimized Clearing Agent. *Cell Rep.* 14, 2718–2732.
- Komatsu, N., Aoki, K., Yamada, M., Yukinaga, H., Fujita, Y., Kamioka, Y., and Matsuda, M. (2011). Development of an optimized backbone of FRET biosensors for kinases and GTPases. *Mol. Biol. Cell* 22, 4647–4656.
- Lee-Hoeflich, S.T., Causing, C.G., Podkowa, M., Zhao, X., Wrana, J.L., and Attisano, L. (2004). Activation of LIMK1 by binding to the BMP receptor, BMPRII, regulates BMP-dependent dendritogenesis. *EMBO J.* 23, 4792–4801.
- Lichtman, J.W., and Colman, H. (2000). Synapse elimination and indelible memory. *Neuron* 25, 269–278.
- Lin, D.M., Wang, F., Lowe, G., Gold, G.H., Axel, R., Ngai, J., and Brunet, L. (2000). Formation of precise connections in the olfactory bulb occurs in the absence of odorant-evoked neuronal activity. *Neuron* 26, 69–80.
- Luo, L. (2002). Actin cytoskeleton regulation in neuronal morphogenesis and structural plasticity. *Annu. Rev. Cell Dev. Biol.* 18, 601–635.
- Ma, L., Wu, Y., Qiu, Q., Scheerer, H., Moran, A., and Yu, C.R. (2014). A developmental switch of axon targeting in the continuously regenerating mouse olfactory system. *Science* 344, 194–197.
- Malun, D., and Brunjes, P.C. (1996). Development of olfactory glomeruli: temporal and spatial interactions between olfactory receptor axons and mitral cells in opossums and rats. *J. Comp. Neurol.* 368, 1–16.
- Mikuni, T., Uesaka, N., Okuno, H., Hirai, H., Deisseroth, K., Bito, H., and Kano, M. (2013). *Arc/Arg3.1* is a postsynaptic mediator of activity-dependent synapse elimination in the developing cerebellum. *Neuron* 78, 1024–1035.
- Mueller, T.D., and Nickel, J. (2012). Promiscuity and specificity in BMP receptor activation. *FEBS Letters* 586, 1846–1859.
- Murai, A., Iwata, R., Fujimoto, S., Aihara, S., Tsuboi, A., Muroyama, Y., Saito, T., Nishizaki, K., and Imai, T. (2016). Distorted Coarse Axon Targeting and Reduced Dendrite Connectivity Underlie Dysosmia after Olfactory Axon Injury. *eNeuro* 3, ENEURO.0242-16.2016.
- Muroyama, Y., Baba, A., Kitagawa, M., and Saito, T. (2016). Olfactory Sensory Neurons Control Dendritic Complexity of Mitral Cells via Notch Signaling. *PLoS Genet.* 12, e1006514.
- Nakahata, Y., and Yasuda, R. (2018). Plasticity of Spine Structure: Local Signaling, Translation and Cytoskeletal Reorganization. *Front. Synaptic Neurosci.* 10, 29.
- Nithianandam, V., and Chien, C.T. (2018). Actin blobs prefigure dendrite branching sites. *J. Cell Biol.* 217, 3731–3746.
- Niwa, R., Nagata-Ohashi, K., Takeichi, M., Mizuno, K., and Uemura, T. (2002). Control of actin reorganization by Slingshot, a family of phosphatases that dephosphorylate ADF/cofilin. *Cell* 108, 233–246.
- Ohashi, K. (2015). Roles of cofilin in development and its mechanisms of regulation. *Dev. Growth Differ.* 57, 275–290.
- Okamoto, K., Nagai, T., Miyawaki, A., and Hayashi, Y. (2004). Rapid and persistent modulation of actin dynamics regulates postsynaptic reorganization underlying bidirectional plasticity. *Nat. Neurosci.* 7, 1104–1112.
- Oser, M., and Condeelis, J. (2009). The cofilin activity cycle in lamellipodia and invadopodia. *J. Cell. Biochem.* 108, 1252–1262.
- Peretto, P., Cummings, D., Modena, C., Behrens, M., Venkatraman, G., Falso, A., and Margolis, F.L. (2002). BMP mRNA and protein expression in the developing mouse olfactory system. *J. Comp. Neurol.* 451, 267–278.
- Podkowa, M., Zhao, X., Chow, C.W., Coffey, E.T., Davis, R.J., and Attisano, L. (2010). Microtubule stabilization by bone morphogenetic protein receptor-mediated scaffolding of c-Jun N-terminal kinase promotes dendrite formation. *Mol. Cell. Biol.* 30, 2241–2250.
- Sakaguchi, R., Leiwe, M.N., and Imai, T. (2018). Bright multicolor labeling of neuronal circuits with fluorescent proteins and chemical tags. *eLife* 7, e40350.
- Saxena, M., Agnihotri, N., and Sen, J. (2018). Perturbation of canonical and non-canonical BMP signaling affects migration, polarity and dendritogenesis of mouse cortical neurons. *Development* 145, dev147157.
- Schelski, M., and Bradke, F. (2017). Neuronal polarization: From spatiotemporal signaling to cytoskeletal dynamics. *Mol. Cell. Neurosci.* 84, 11–28.
- Straub, C., Granger, A.J., Saulnier, J.L., and Sabatini, B.L. (2014). CRISPR/Cas9-mediated gene knock-down in post-mitotic neurons. *PLoS ONE* 9, e105584.
- Sunagawa, G.A., Sumiyama, K., Ukai-Tadenuma, M., Perrin, D., Fujishima, H., Ukai, H., Nishimura, O., Shi, S., Ohno, R.I., Narumi, R., et al. (2016). Mammalian Reverse Genetics without Crossing Reveals Nr3a as a Short-Sleeper Gene. *Cell Rep.* 14, 662–677.
- Tasaka, G., Negishi, M., and Oinuma, I. (2012). Semaphorin 4D/Plexin-B1-mediated M-Ras GAP activity regulates actin-based dendrite remodeling through Lamellipodin. *J. Neurosci.* 32, 8293–8305.
- Tsunekawa, Y., Terhune, R.K., Fujita, I., Shitamukai, A., Suetsugu, T., and Matsuzaki, F. (2016). Developing a *de novo* targeted knock-in method based on *in utero* electroporation into the mammalian brain. *Development* 143, 3216–3222.
- Tu, X., Yasuda, R., and Colgan, L.A. (2020). Rac1 is a downstream effector of PKC $\alpha$  in structural synaptic plasticity. *Sci. Rep.* 10, 1777.
- Uesaka, N., Uchigashima, M., Mikuni, T., Nakazawa, T., Nakao, H., Hirai, H., Aiba, A., Watanabe, M., and Kano, M. (2014). Retrograde semaphorin signaling regulates synapse elimination in the developing mouse brain. *Science* 344, 1020–1023.
- Uesaka, N., Abe, M., Konno, K., Yamazaki, M., Sakoori, K., Watanabe, T., Kao, T.H., Mikuni, T., Watanabe, M., Sakimura, K., and Kano, M. (2018). Retrograde Signaling from Progranulin to Sort1 Counteracts Synapse Elimination in the Developing Cerebellum. *Neuron* 97, 796–805.e5.

- Valnegri, P., Puram, S.V., and Bonni, A. (2015). Regulation of dendrite morphogenesis by extrinsic cues. *Trends Neurosci.* *38*, 439–447.
- Watanabe, M., and Kano, M. (2011). Climbing fiber synapse elimination in cerebellar Purkinje cells. *Eur. J. Neurosci.* *34*, 1697–1710.
- Wen, Z., Han, L., Bamberg, J.R., Shim, S., Ming, G.L., and Zheng, J.Q. (2007). BMP gradients steer nerve growth cones by a balancing act of LIM kinase and Slingshot phosphatase on ADF/cofilin. *J. Cell Biol.* *178*, 107–119.
- Wong, R.O.L., and Ghosh, A. (2002). Activity-dependent regulation of dendritic growth and patterning. *Nat. Rev. Neurosci.* *3*, 803–812.
- Yasuda, M., Nagappan-Chettiar, S., Johnson-Venkatesh, E.M., and Umemori, H. (2021). An activity-dependent determinant of synapse elimination in the mammalian brain. *Neuron* *109*, 1333–1349.e6.
- Zebda, N., Bernard, O., Bailly, M., Welti, S., Lawrence, D.S., and Condeelis, J.S. (2000). Phosphorylation of Adf/Cofilin Abolishes Egf-Induced Actin Nucleation at the Leading Edge and Subsequent Lamellipod Extension. *J. Cell Biol.* *151*, 1119–1128.
- Zimmerman, L.B., De Jesús-Escobar, J.M., and Harland, R.M. (1996). The Spemann organizer signal noggin binds and inactivates bone morphogenetic protein 4. *Cell* *86*, 599–606.

STAR★METHODS

KEY RESOURCES TABLE

REAGENT or RESOURCE	SOURCE	IDENTIFIER
<b>Antibodies</b>		
Normal donkey serum	Sigma	Cat#D9663
Rat anti-ER-TR7	Abcam	Cat#ab51824, RRID:AB_881651
Rabbit Anti-GFP	Invitrogen	Cat#A11122, RRID:AB_221569
Rabbit Anti-Eomes/Tbr2	Abcam	Cat#ab23345, RRID:AB_778267
Mouse Anti-Tbx21	Abcam	Cat#ab91109, RRID:AB_2050371
Alexa 488-conjugated donkey anti-rat IgG	Thermo Fisher Scientific	Cat# A-21208; RRID:AB_2536180
Alexa 488-conjugated donkey anti-rabbit IgG	Thermo Fisher Scientific	Cat# A-21206; RRID:AB_2536180
Alexa 555-conjugated donkey anti-rabbit IgG	Thermo Fisher Scientific	Cat# A-31572; RRID:AB_2536180
Alexa 555-conjugated donkey anti-mouse IgG	Thermo Fisher Scientific	Cat# A-31570; RRID:AB_2536180
<b>Chemicals, peptides, and recombinant proteins</b>		
Paraformaldehyde	Nacalai Tesque	Cat# 26126-25
Low-melting point agarose	Thermo Fisher Scientific	Cat# 16520-100
OCT compound	Sakura	Ca# 4583
Saponin	Nacalai Tesque	Cat# 30502-42
Omnipaque 350	Daiichi-Sankyo	N/A
DAPI solution	DOJINDO	Cat# D523
Nembutal	Dainippon Sumitomo Pharma	N/A
Somnopenyl	Kyoritsu Seiyaku	N/A
Ketamine	Daiichi-Sankyo	N/A
Xylazine	Bayer	N/A
RNeasy Plus Mini Kit	Quiagen	Cat# 74134
SuperScript IV	Thermo Fisher Scientific	Cat#18090010
Oligo(dT)20 primer	Invitrogen	Cat#18418020
Low Input Quick Amp Gene Expression Labeling Kits	Agilent	Cat#5190-2331
SuperPrint G3 Mouse GE 8x60K Microarray Kit Ver 2.0	Agilent	Cat# G4852
PowerUP SYBR Green Master Mix	Thermo Fisher Scientific	Cat# A25742
NMDA	Nacalai	Cat#22034-1
Glycine	Sigma	Cat#G7126-100G
AP5	Sigma	Cat# A5282
AMPA	TOCRIS	Cat#0169
TTX	Abcam	Cat# ab120055
Alexa Fluor 555 Tyramide Reagent	Thermo Fisher Scientific	Cat#B40955
<b>Critical commercial assays</b>		
RNA scope probe Bmp2	Advanced Cell Diagnostics	Cat#406661
RNA scope probe Bmp4	Advanced Cell Diagnostics	Cat#401301
RNA scope 2.5HD Reagent kit Brown	Advanced Cell Diagnostics	Cat#322300
<b>Deposited data</b>		
Raw image data	This paper	<a href="https://doi.org/10.24631/ssbd.repos.2021.04.001">https://doi.org/10.24631/ssbd.repos.2021.04.001</a>
NeuroLucida tracing data	This paper	<a href="http://neuromorpho.org/">http://neuromorpho.org/</a>

(Continued on next page)

**Continued**

REAGENT or RESOURCE	SOURCE	IDENTIFIER
Microarray data	This paper	<a href="https://www.ncbi.nlm.nih.gov/geo/query/acc.cgi?acc=GSE171875">https://www.ncbi.nlm.nih.gov/geo/query/acc.cgi?acc=GSE171875</a>
<b>Experimental models: organisms/strains</b>		
ICR mice	Japan SLC	RRID:MGI:5462094
C57BL/6N mice	Japan SLC	RRID:MGI:5295404
Thy1-GCaMP6f (C57BL/6J-Tg(Thy1-GCaMP6f)GP5.11Dkim/J)	The Jackson Laboratory	Cat# JAX:024339; RRID:IMSR_JAX:024339
<b>Oligonucleotides</b>		
Thy1-GCaMP6f genotyping primer, forward: CTGACTGAAGAGCAGATCGCAGAAT	<a href="#">Dana et al., 2014</a>	N/A
Thy1-GCaMP6f genotyping primer, reverse: GCAGCGTATCCACATAGCGTAAAAG	<a href="#">Dana et al., 2014</a>	N/A
qPCR primers	This paper, See <a href="#">Table S5</a>	N/A
<b>Recombinant DNA</b>		
pCAG-FLPo	<a href="#">Fujimoto et al., 2019</a>	Addgene # 125576
pCAFNF-tdTomato	<a href="#">Fujimoto et al., 2019</a>	Addgene # 125575
pCAX-Cas9	<a href="#">Tsunekawa et al., 2016</a>	Gift from Dr. Matsuzaki
Bmpr2 gRNA#1	This paper	Addgene # 163388
Bmpr2 gRNA#2	This paper	Addgene # 163389
Bmpr2 gRNA#3	This paper	Addgene # 163390
pCAG-Bmpr2	This paper	Addgene # 163408
pCAG-Bmpr2ΔKinase	This paper	Addgene # 163411
pCAG-Bmpr2ΔTail	This paper	Addgene # 163412
pCAG-Bmpr2ΔEC	This paper	Addgene # 163413
pCAG-Limk1	This paper	Addgene # 163414
pCAG-Bmpr2	This paper	Addgene # 163403
pCAG-Bmpr2ΔKinase	This paper	Addgene # 163404
pCAG-Bmpr2ΔTail	This paper	Addgene # 163405
pCAG-Bmpr2ΔEC	This paper	Addgene # 163406
pCAG-Noggin	This paper	Addgene # 163586
pCAG-Bmp2	This paper	Addgene # 163587
pCAG-Bmp4	This paper	Addgene # 163588
pCAG-Bmp5	This paper	Addgene # 163589
pCAG-Bmp6	This paper	Addgene # 163590
pCAG-Bmp7	This paper	Addgene # 163591
pCAG-Bmp8a	This paper	Addgene # 163592
pCAG-Bmp15	This paper	Addgene # 163594
pCAG-Gdf5	This paper	Addgene # 163596
pCAG-Gdf6	This paper	Addgene # 163598
pCAG-Gdf7	This paper	Addgene # 163597
pCAG-Gdf9	This paper	Addgene # 163599
pCAFNF-Rhoa	This paper	Addgene # 163605
pCAFNF-Cdc42	This paper	Addgene # 163606
pCAFNF-Rac1	This paper	Addgene # 163607
Limk1 gRNA#1	This paper	Addgene # 163391
Limk1 gRNA#2	This paper	Addgene # 163392
Limk1 gRNA#3	This paper	Addgene # 163393
pCAG-Pak1	This paper	Addgene # 163600
pCAGGS-RaichuEV-Rac1	<a href="#">Komatsu et al., 2011</a>	Gift from Dr. Aoki

(Continued on next page)

**Continued**

REAGENT or RESOURCE	SOURCE	IDENTIFIER
pCAG-RaichuEV-Rac1 (T17N)	This paper	Addgene # 164902
pCAG-rtTA	This paper	Addgene # 163601
pBS-TRE-mTurquoise2-WPRE	<a href="#">Sakaguchi et al., 2018</a>	Addgene # 104103
pBS-TRE-cofilin1(S3A)-P2A-mTurquoise2	This paper	Addgene # 163610
Slingshot1 gRNA#1	This paper	Addgene # 163394
Slingshot1 gRNA#2	This paper	Addgene # 163395
Slingshot1 gRNA#3	This paper	Addgene # 163396
Slingshot2 gRNA#1	This paper	Addgene # 163397
Slingshot2 gRNA#2	This paper	Addgene # 163398
Slingshot2 gRNA#3	This paper	Addgene # 163399
Slingshot3 gRNA#1	This paper	Addgene # 163400
Slingshot3 gRNA#2	This paper	Addgene # 163401
Slingshot3 gRNA#3	This paper	Addgene # 163402
pCAG-Slingshot1	This paper	Addgene # 163602
Grin1 gRNA#1	This paper	Addgene # 169789
Grin1 gRNA#2	This paper	Addgene # 169790
Grin1 gRNA#3	This paper	Addgene # 169791
pCAFNF-ECFP-actin	This paper	Addgene # 169787
pCAFNF-Venus-actin	This paper	Addgene # 169788
pCAFNF-LifeAct-EGFP	This paper	Addgene # 163608
pCAFNF-EGFP	This paper	Addgene # 163609
Eomes gRNA#1	This paper	Addgene # 170834
Eomes gRNA#2	This paper	Addgene # 170835
Eomes gRNA#3	This paper	Addgene # 170836
Tbx21 gRNA#1	This paper	Addgene # 170837
Tbx21 gRNA#2	This paper	Addgene # 170838
Tbx21 gRNA#3	This paper	Addgene # 170839
pCAFNF-PSD $\Delta$ 1.2-EGFP	<a href="#">Fujimoto et al., 2019</a>	Addgene # 125581
pCAG-Bmpr2 $\Delta$ 751-813aa	This paper	Addgene # 163603
Bax gRNA#1	This paper	Addgene # 171827
Bax gRNA#2	This paper	Addgene # 171828
Bax gRNA#3	This paper	Addgene # 171829
pCAG-cofilin S3A	This paper	Addgene # 163604

**Software and algorithms**

ImageJ	<a href="https://imagej.nih.gov/ij/">https://imagej.nih.gov/ij/</a>	RRID:SCR_003070
NeuroLucida	MBF Bioscience	RRID:SCR_001775
Huygens software	Scientific Volume Imaging	RRID:SCR_014237
Prism7	GraphPad	RRID:SCR_002798
Leica Application Suite X	Leica	RRID:SCR_013673
Olympus Fluoview FV10-ASW	Olympus	RRID:SCR_014215

**Other**

Electroporator	BEX	Cat# CUY21EX
Forceps-type electrodes	BEX	Cat# LF650P3
Microslicer	Dosaka	Cat# PRO7
Cryostat	Leica	Cat# CM3050S
Confocal microscope SP8	Leica	N/A
ABI7500	Applied Biosystems	N/A
FV1000MPE	Olympus	N/A
Insight DS Dual	Spectra-Physics	N/A

(Continued on next page)

**Continued**

REAGENT or RESOURCE	SOURCE	IDENTIFIER
XLPLN25XWMP	Olympus	N/A
DMI6000B	Leica	N/A
DNA microarray scanner G2505C	Agilent	N/A

**RESOURCE AVAILABILITY**

**Lead contact**

Further information and requests for resources and reagents should be directed to and will be fulfilled by the lead contact, Takeshi Imai ([imai.takeshi.457@m.kyushu-u.ac.jp](mailto:imai.takeshi.457@m.kyushu-u.ac.jp)).

**Materials availability**

Newly generated plasmids are available from Addgene (See [key resources table](#)).

**Data and code availability**

All the image data have been deposited to SSBD:repository (<https://doi.org/10.24631/ssbd.repos.2021.04.001>). Microarray data have been deposited to NCBI GEO: GSE171875. NeuroLucida tracing data will be deposited to [NeuroMorpho.Org](http://neuromorpho.org) (<http://neuromorpho.org>). Numerical data for all graphs are included in [Table S2](#). No new program codes were generated in this study. Requests for additional data should be directed to and will be fulfilled on reasonable request by the Lead Contact, Takeshi Imai.

**EXPERIMENTAL MODEL AND SUBJECT DETAILS**

**Mice**

All animal experiments were approved by the Institutional Animal Care and Use Committee (IACUC) of the RIKEN Kobe Branch and Kyushu University. *Thy1-GCaMP6f* Tg (line GP5.11) (JAX #024339) ([Dana et al., 2014](#)) has been described previously. ICR mice (Japan SLC, RRID: MGI: 5652524) were used for in utero electroporation. C57BL/6N mice were used for qPCR and *in situ* hybridization. Both male and female mice were analyzed (P1-6). For anatomical and histological analyses, mice were deeply anesthetized by intraperitoneal injection of overdose Nembutal (Dainippon Sumitomo Pharma) or Somnopentyl (Kyoritsu Seiyaku) and perfused with phosphate buffered saline (PBS) for in utero electroporation samples and 4% paraformaldehyde (PFA) in PBS for other samples. Dissected brains were post-fixed with 4% PFA in PBS at 4°C overnight. For inducible gene expression by the Tet-on system, drinking water containing doxycycline (2mg/mL, Sigma-Aldrich, # D9891) and sucrose (10% w/v) was administered from P0.

**METHOD DETAILS**

**CRISPR/Cas9**

A procedure for gRNA construction is shown in [Figure S1A](#). pCAX-Cas9 and gRNA backbone vector were kind gifts from F. Matsuzaki ([Tsunekawa et al., 2016](#)). For the CRISPR/Cas9-based KO system, the three gRNAs that target different exons were designed to increase KO efficiency ([Sunagawa et al., 2016](#)). The gRNA sequences were designed by Optimized gRNA design (<https://zlab.bio/guide-design-resources>) or CHOPCHOP (<https://chopchop.cbu.uib.no/>). The gRNA sequences are shown in [Table S1](#). Target sequences were amplified with forward and reverse oligonucleotides by PCR and inserted into the gRNA backbone vector at AflII sites ([Tsunekawa et al., 2016](#)).

**Plasmids**

ORF sequences were amplified by PCR from P6 mouse OB or OE cDNA. Because *Gdf7* contains GC rich sequences, we could not amplify the ORF from cDNA. Instead, we designed a synthetic *Gdf7* gene with lower GC contents (GeneArt, ThermoFisher). Amplified genes were subcloned into *pCAG*, *pCA-FNF*, or *pTRE* vector. FLPo (addgene #13793, a gift from P. Soriano) was amplified by PCR and subcloned into a pCAG vector. Truncated versions of *Bmpr2* (NM\_007561.4) encode the following amino acid sequences; *Bmpr2ΔKinase* (1-201 and 501-1038 aa.), *Bmpr2ΔTail* (1-529 aa.), *Bmpr2ΔEC* (1-26 and 151-1038 aa.), and *Bmpr2Δ751-813aa* (1-750 and 814-1038 aa.). gRNA-resistant *Bmpr2* (Designated *Bmpr2<sup>†</sup>*) was generated by PCR-mediated mutagenesis and has the following sequences on the gRNA-targeting sequences; CaagtCTaCaGacCaTTcaGa, agtAAGgGatcaACaTGcTAcGG, and aGgTAtGGtGcTGTtTAcAAgGG (small characters are substituted nucleotides). A FRET sensor, RaichuEV-Rac1 ([Komatsu et al., 2011](#)), is a kind gift from K. Aoki. Newly generated plasmids have been deposited to Addgene (See [Key resources table](#)).

### In utero electroporation

To sparsely label neurons, pCAG-Flpo (Addgene #125576, 3–10 ng/ $\mu$ L) and pCAFNF-tdTomato (Addgene#125575, 1  $\mu$ g/ $\mu$ L) were used. For CRISPR/Cas9-based KO, three types of gRNA plasmids (0.1  $\mu$ g/ $\mu$ L each) and pCAX-Cas9 (0.1  $\mu$ g/targeted gene/ $\mu$ L) were used (Tsunekawa et al., 2016). For Tet-On system, pCAG-rtTA (0.25  $\mu$ g/ $\mu$ L) was used. For actin FRET, pCAFNF-ECFP-Actb (0.5 or 0.7  $\mu$ g/ $\mu$ L) and pCAFNF-ECFP-Actb (1.5 or 2.1  $\mu$ g/ $\mu$ L) were used, respectively. For other plasmids, concentration was 1  $\mu$ g/ $\mu$ L (see Table S4 for detailed conditions). When two plasmids were co-electroporated at 1  $\mu$ g/ $\mu$ L each, co-electroporation rate was approximately 90% (data not shown). In utero electroporation was performed as described previously (Fujimoto et al., 2019; Muroyama et al., 2016; Sakaguchi et al., 2018). Pregnant mice carrying E12 embryos were anesthetized with ketamine (64–80 mg/kg) and xylazine (11.2–14 mg/kg). The uterine horns were exposed by abdominal incision. A plasmid cocktail was injected into the lateral ventricle of the embryos using a glass capillary. Electric pulses (a 10ms single poration pulse at 72V followed by five 50 ms duration, 34V driving pulses with a 950 ms interval) were delivered by a CUY21EX electroporator (BEX, # CUY21EX) and forcep-type electrodes (3 mm diameter, #LF650P3, BEX). After the surgery, anesthetized mice were kept on the heating pad (IKEDA scientific, #IP-4530) until they wake up.

### Single-cell cDNA preparation and microarray

Mitral cells were labeled with EYFP using *in utero* electroporation. At P3 or P6, the OB was minced in Ca<sup>2+</sup>-free Ringer's solution (138mM NaCl, 2mM MgCl<sub>2</sub>, 2mM sodium pyruvate, 9.4mM glucose, 2mM EGTA and 5mM HEPES, pH7.4). Minced OB was incubated with 0.88U/mL Dispase (Invitrogen), 200 U/mL Collagenase type II, and 0.1 mg/mL DNase I (Roche) for 20 minutes at 37°C. The sample was centrifuged at 1k rpm for 5 minutes and the pellet was resuspended in Ca<sup>2+</sup> free Ringer's solution. After repeating this washing procedure again, 0.1% bovine serum albumin and 0.05 mg/mL DNase solution were mixed gently. The sample was placed on a coverslip and the EYFP-expressing mitral cells were collected manually with a glass capillary, a micro-manipulator, TransferMan NK2 (Eppendorf), and a microinjector, CellTram vario (Eppendorf), equipped to an inverted fluorescence microscope, DMI6000B (Leica). The picked single cell was rinsed in a drop of 0.1% bovine serum albumin/ Ringer's solution (Ca<sup>2+</sup> free Ringer's solution contained 2mM CaCl<sub>2</sub>), transferred to 0.4  $\mu$ L of RNase free H<sub>2</sub>O in PCR tube, snap-frozen in liquid nitrogen, and stored at –80°C until use. Single-cell cDNA synthesis and amplification was performed as described previously (Imai et al., 2009). Briefly, a T7 promoter was attached to the 3' end and the total cDNA was PCR-amplified (30 cycles). The quality of PCR-amplified cDNA was assessed by agarose gel electrophoresis. Samples with sufficient yields, containing *EYFP* and *pcdh21* transcripts (determined by secondary PCR for *EYFP* and *pcdh21*) were used in subsequent analyses. Samples from 10 neurons were pooled for each hybridization experiment. Cy3 labeling was performed with T7 RNA polymerase using Agilent Low RNA Input Linear Amplification Kit following manufacturer's instructions (Agilent). The microarray was performed using the SuperPrint G3 Mouse GE 8x60K Microarray Kit Ver 2.0 (Agilent, #G4852) and a DNA microarray scanner, G2505C (Agilent). The data were analyzed with Microsoft Excel. Raw data have been deposited to the NCBI Gene Expression Omnibus (GEO) with accession number, #GSE171875.

### Clearing with SeeDB2

PFA-fixed brains were rinsed in PBS and then embedded in 2% agarose gel. Samples were then sliced by a microslicer (Dosaka EM, # PRO7) at 2 mm thickness for CRISPR/Cas9 screening, 0.5 mm thickness for LifeAct-EGFP and PSD $\Delta$ 1.2-EGFP samples, and 1 mm thickness for the others. Brain slices were then stained with DAPI and cleared with SeeDB2G as described previously (Ke and Imai, 2018; Ke et al., 2016). For immunostaining, slices were incubated in blocking solution (2% saponin, 0.25% fish gelatin, 0.5% skim milk, 0.5% Triton X-100 and 0.05% sodium azide in PBS) overnight. Slices were then incubated with primary antibody diluted in the blocking solution for 2 days at room temperature with gentle rotation. Anti-Eomes (abcam, #ab23345, 1:250) and Tbx21 (abcam, #ab91109, 1:250) were used. For Tbx21 staining, brains were treated by autoclave at 105°C for 1 min before slicing, and rabbit anti-GFP (Invitrogen, #A11122, 1:250) was also used to label GFP positive neurons. Slices were then washed with 0.1% Triton X-100 / PBS for 1.5 hours 3 times and incubated with Alexa Fluor 555-conjugated donkey anti-rabbit IgG (1:250, ThermoFisher, #A-31572) and/or Alexa Fluor 555-conjugated donkey anti-mouse IgG (1:250, ThermoFisher, #A-31570) diluted in the blocking solution overnight with gentle rotation. After washing twice with 0.1% Triton X-100 / PBS for 2 hours, slices were incubated in Omnipaque 350 (Sankyo) for clearing overnight with gentle rotation.

### Confocal imaging and image processing

Cleared samples were mounted on glass slides with 0.5, 1, or 2 mm thick silicone rubber spacer as described (Ke and Imai, 2018). Samples were imaged with a 2-photon microscope (Olympus, FV1000MPE) for initial KO screening, and an inverted confocal microscope (Leica, SP8) for others. A water-immersion 25x objective lens (Olympus, XLPLN25XWMP, NA 1.05) was used for 2-photon imaging. A multi-immersion 20x (HC PL APO 20x/0.75 IMM CORR CS2, NA 0.75) and a glycerin-immersion 63x (HC PL APO 63x/1.3 Gly CORR CS2, NA 1.3) objective lenses were used for confocal imaging. High resolution images of LifeAct and PSD puncta were acquired with HyVolution package of a confocal microscope Leica TCS SP8 (Leica Microsystems) and Huygens software (Scientific Volume Imaging). The voxel size was approximately 40 nm in x-y and 120 nm in z-axis.

### Quantification of neuronal morphology

Neuronal morphology was analyzed with Neurolucida software (MBF Bioscience). Neurons labeled with tdTomato in the mitral cell layer were analyzed. Analysis was confined to mitral cells located in the medial side of the OB. We sometimes found neurons with

small soma and neurites with dendritic spines that did not contact a glomerulus; these are granule cells and were excluded from subsequent analysis. Glomeruli were identified with DAPI staining. Neuronal tracing and analysis were not blinded; however, we comprehensively analyzed all the neurons in a volume that meets the above criteria to avoid any biases in quantification.

Regarding the quantification of LifeAct signals, we obtained mitral cell images that were isolated from other labeled cells, along the entire in the OB. Brightly labeled mitral cells whose dendrites orient to glomeruli in the external plexiform layer (EPL) were comprehensively analyzed. Signal intensities within 30  $\mu\text{m}$  from the tips of dendrites in maximum projection images were measured using ImageJ. After thresholding, the mean signal intensity per area was compared between dendrites within and outside glomeruli.

For PSD puncta analysis, we collected the mitral cell data from the entire OB. For tuft volume and PSD puncta analysis, high-resolution images processed by HyVolution software (Huygens) were used. For tuft volume analysis, the tdTomato channel images were thresholded by the ImageJ pre-installed threshold algorithm IsoData or Triangle depending on the image brightness. For puncta analysis, maximum projection images of the PSD $\Delta$ 1.2-EGFP channel were subtracted by the tdTomato channels in which the brightness was adjusted to EGFP on the shaft. Then, a threshold was set at a level at which there is no or at most one punctum in the shaft. The tuft volume was automatically analyzed using an ImageJ plugin (Voxel Counter) in 3D images. The number and area of PSD puncta were measured with maximal intensity projections using ImageJ particle analysis.

### qPCR

Total RNA was extracted from OE and OB samples at P3 and P6 using the RNeasy Plus Mini Kit (QIAGEN, #74134). In order to collect sufficient amounts of RNA, samples from 5 mice were pooled for RNA extraction. In total, 3 pooled RNA samples from 15 mice were prepared. cDNAs were synthesized with SuperScript IV (ThermoFisher, #18090010) using Oligo(dT)20 primers (ThermoFisher, #18418020). qPCR primers are described in Table S5. For real-time PCR, PowerUP SYBR Green (ThermoFisher, #A25742) and ABI7500 (Applied Biosystems) were used. PCR efficiencies of each primer were estimated by qPCR of plasmids encoding each target gene. Data were analyzed using Excel (Microsoft). We calculated amounts of mRNA based on Ct value and PCR efficiency. The calculated values were normalized by *Actb* gene.

### In situ hybridization (RNA scope)

RNA scope was used for *in situ* hybridization following manufacturer's instructions. *Bmp2* (#406661) and *Bmp4* (#401301) probes were purchased from Advanced Cell Diagnostics. To avoid tissue shrinkage during cryoprotection, 15% fructose was used instead of 30% sucrose. In double staining experiments, conventional immunohistochemistry was performed after RNA scope. Briefly, after Amp6 of RNA scope 2.5HD Reagent kit Brown (Advanced Cell Diagnostics, #322300), sections were incubated with AlexaFluor555-Tyramide reagent (Thermo Fisher Scientific, #B40923). After washing in PBS, sections were fixed with 4% PFA/PBS for 15 min, washed in PBS, and blocked with 5% donkey serum for 30 min. Then sections were incubated with anti-ER-TR7 (1:200, abcam, # ab51824) for 1 hour at room temperature and then washed three times in PBS. Finally, sections were incubated with DAPI (1:200, DOJINDO, # 340-07971) and a secondary antibody conjugated with AlexaFluor 488 (1:200, Thermo Fisher Scientific, # A-21208) for 1 hour at room temperature. After washing, sections were mounted using ProLong Gold (Thermo Fisher Scientific, #P36930). Leica DMI6000B was used for image acquisition.

### Ca<sup>2+</sup> and FRET imaging

Thy1-GCaMP6f mice were used for Ca<sup>2+</sup> imaging. For FRET imaging, pCAG-RaichuEV-Rac1 (Komatsu et al., 2011), or pCAFNF-ECFP-actin and -Venus-actin (Okamoto et al., 2004) were introduced at E12 by *in utero* electroporation. FRET and Ca<sup>2+</sup> imaging was performed at P3-5. Mice were anesthetized on ice and decapitated. The brain was immediately harvested and placed in cold artificial corticospinal fluid (ACSF: 125 mM NaCl, 3 mM KCl, 1.25 mM NaH<sub>2</sub>PO<sub>4</sub>, 2 mM CaCl<sub>2</sub>, 1 mM MgCl<sub>2</sub>, 25 mM NaHCO<sub>3</sub>, and 25 mM glucose). The brain was embedded in 2% agarose gel and sliced using a microslicer (Dosaka) at 300  $\mu\text{m}$  thickness. An OB slice was placed on a custom-made silicone chamber (Fujimoto et al., 2019) and fixed with a nylon mesh (Warner Instrument, # 64-0198). The chamber was set under a 2-photon microscope (Olympus, FV1000MPE) equipped with a water-immersion 25x objective lens (Olympus, XLPLN25XWMP, NA = 1.05, WD = 2.0). Before the imaging, the OB slice was perfused with oxygenized ACSF at least for 2 hours at 27°C for recovery. The excitation laser was tuned to 920 nm for Ca<sup>2+</sup> imaging and 840 nm for FRET imaging. Dichroic mirrors FV10-MRVGR/XR (Olympus, #FP1NDF4VGRXR) and FV10-MRC/YW (Olympus, #FP1NDF4CY-G) were used for Ca<sup>2+</sup> and FRET imaging, respectively. Emitted signals were detected with GaAsP detectors. Images were acquired every 0.5 s for Ca<sup>2+</sup>, 5 s for Rac1 FRET imaging, and 2 min for actin FRET imaging. The resolution of Ca<sup>2+</sup> and FRET imaging was 1.988 and 0.497  $\mu\text{m}/\text{pixel}$  respectively. Following drugs were used: 100 or 30  $\mu\text{M}$  NMDA (Nacalai, Cat #22034-1), 100  $\mu\text{M}$  AP5 (Sigma-Aldrich, #A5282), 100  $\mu\text{M}$  AMPA (TOCRIS, #0169), 1  $\mu\text{M}$  TTX (abcam, #ab120055), and 40 or 12  $\mu\text{M}$  Glycine (Sigma, #G7126-100G). Glycine was co-applied with NMDA and AMPA. TTX was applied 7-20 min before NMDA or AMPA stimulation. Samples drifted by the drug application were excluded from subsequent data analysis. Data were analyzed with ImageJ. Briefly, small drifts by drug application were corrected by ImageJ plugin (Correct 3D drift) when possible. Background signals were removed by thresholding. For the analysis of Ca<sup>2+</sup> imaging data, the F0 was calculated as the average before stimulation (2 or 4 min). For the FRET data, the YFP/CFP ratio was calculated at each frame and then normalized by the average value before stimulation at each pixel to create representative images, or, at the ROI level for time courses and quantification. To calculate the averaged  $\Delta F/F$  and  $\Delta$  normalized YFP/CFP for RaichuEV-Rac1, a mean value for 3 minutes after stimulation onset was subtracted by the mean value for 1 minute before

stimulation onset. For actin FRET imaging, a mean value for 14–18 min was subtracted by the mean value for 20 minutes before stimulation.

### QUANTIFICATION AND STATISTICAL ANALYSIS

Excel and Prism7 were used for statistical analysis. Sample sizes for dendrite quantification were determined based on pilot experiments (using G Power). The number of neurons is described within figures, and number of animals is described in [Table S2](#). P values are summarized in [Table S3](#). Data distribution was tested by Shapiro-Wilk test and D'Agostino-Pearson test.  $\chi^2$ -tests were used in [Figures 1, 2, 3, 4, 5, 7, and S1–S3](#). Mitral cells with no primary dendrites were excluded from the statistical tests because  $\chi^2$ -tests compared the single versus multiple dendrite population. For the multiple comparison of  $\chi^2$ -tests, Bonferroni correction was used. A One-way ANOVA was used in [Figures 6, 7I, and S2](#) with Tukey's post hoc test for multiple comparison. Kruskal-Wallis test with Dunn's multiple comparison was used in [Figures 7L and S2K](#). Mann Whitney test was used in [Figures S2B–S2E](#). Data inclusion/exclusion criteria are described in each [Method details](#) section.

Cell Reports, Volume 35

**Supplemental information**

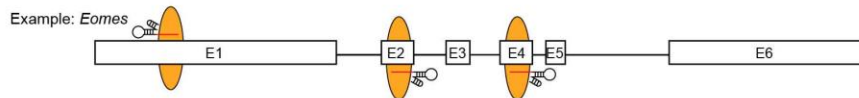
**BMPR-2 gates activity-dependent stabilization  
of primary dendrites during mitral cell remodeling**

**Shuhei Aihara, Satoshi Fujimoto, Richi Sakaguchi, and Takeshi Imai**

## SUPPLEMENTAL FIGURES

**A** 1) Search for target sequences.

2) Pick up 3 target sequences. They should be on different exons.



3) Design primers containing a target sequence and a flanking sequence.

e.g. if a target sequence is **ACTACAGCGACACCGTGCATGGG**  
 Forward primer: **TTATATATCTTTGTGGAAGGACGAAACACC****gCTACAGCGACACCGTGCAT**  
 Reverse primer: **ATTTAACTTGTCTATTTCTAGCTCTAAAAC****ATgCACGGTGTGCGTGTAG**  
 (5'-3')

4) Amplify primers by PCR and insert it into the guide RNA backbone at AflII site using Gibson assembly.

5) Prepare endotoxin-free plasmids and perform in utero electroporation.

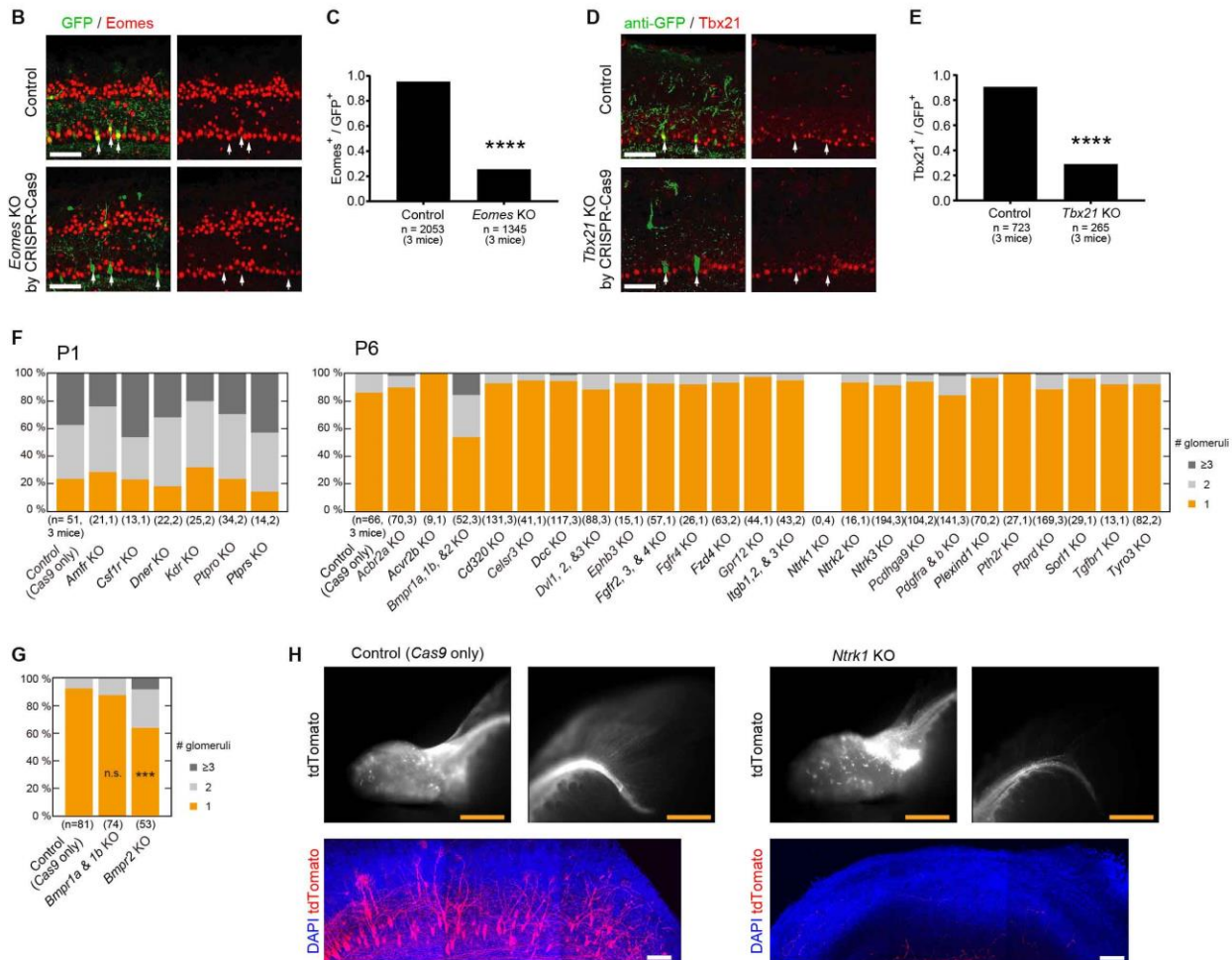


**Figure S1. CRISPR/Cas9-based knock-out screening, Related to Figure 1.**

**(A)** A procedure for gRNA construction. It takes approximately 4 days to prepare a gRNA

plasmid.

**(B-E)** The efficiency of our CRISPR/Cas9 KO screening. We have chosen *Eomes* (*Tbr2*) and *Tbx21*, because they are specifically expressed in mitral/tufted cells and their antibodies are available. For both genes, we have designed gRNAs in the coding region as described in **(A)**. We have automatically picked the 3 best gRNAs as suggested by the gRNA designing program. An EGFP expression vector was co-expressed with CRISPR/Cas9 plasmids. Immunostaining demonstrated a KO efficiency of 70.6% on average. \*\*\*\*  $p < 0.001$  ( $\chi^2$  test). Scale bars, 100  $\mu\text{m}$ .

**(F)** Candidate cell surface receptors tested in this study. Based on the single-cell microarray data for mitral cells, we have chosen cell surface receptors. We performed CRISPR/Cas9-based KO screening for these receptor genes in single, double, or triple KOs in the initial screening. We could not find mitral cell somata for *Ntrk1* KO samples, while labeled axons were found. It is possible that retrograde NGF signals received by Trk-A (encoded by *Ntrk1*) are essential for mitral cell survival (Ginty and Segal, 2002).

**(G)** After identifying defective dendrite pruning in the *Bmpr1a/1b/2* triple KO experiment, we performed further KO experiments, and identified *Bmpr2* as a critical gene for dendrite remodeling. n.s., non-significant, \*\*\*  $p < 0.001$  ( $\chi^2$  test with Bonferroni correction, vs control).

**(H)** *Ntrk1* KO. Top panels show epifluorescence images of OB and mitral cell axons in the lateral olfactory tract. Bottom panels are 400  $\mu\text{m}$  z-stack OB images acquired with 2-photon microscopy. Top and bottom are from the same samples. Axons were observed, but mitral cell somata were not seen in the OB. Scale bars, 1 mm (Top) and 100  $\mu\text{m}$  (bottom).

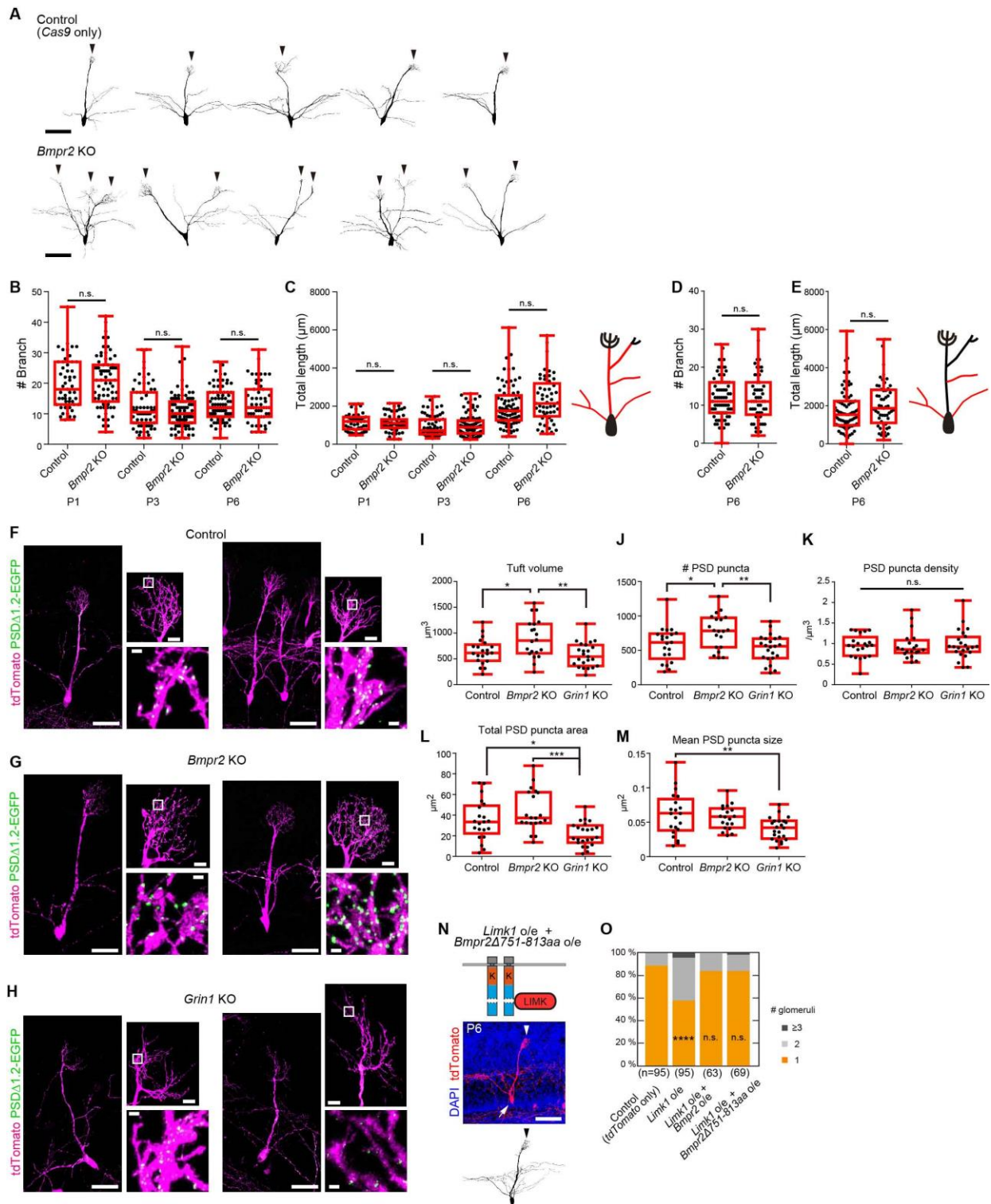


**Figure S2. Quantitative analysis of dendrite development in mitral cells, Related to Figure 1 and 3.**

(A) Representative traces of control and *Bmpr2* KO mitral cells at P6. Scale bars, 100 μm.  
 (B, C) Total numbers of dendritic branches and length were quantified in control and *Bmpr2* KO

mitral cells at P1, 3, and 6. Dendritic tufts were excluded from the quantification. There was no significant difference between control and *Bmpr2* KO. n = 51, 72, 68, 101, 80, 53 cells, respectively. n.s., non-significant (Mann-Whitney test). In the boxplots, whiskers represent the maximum and minimum, boxes represent the inter-quartile range, and horizontal lines represent the median. Black dots represent individual mitral cells.

**(D, E)** Total number of lateral dendrites and their length. n = 80 and 53 cells, respectively. n.s., non-significant (Mann-Whitney test).

**(F-H)** Representative images of dendritic tufts and PSD puncta. PSD puncta were visualized by PSD $\Delta$ 1.2-EGFP which are localized at the postsynaptic density without side effects. *Bmpr2* or *Grin1* were simultaneously knocked out. Low-magnification images of the whole cell (left), intermediate magnification images of the dendritic tufts (right top), and high-magnification images of PSD puncta (right bottom) are shown. White boxes indicate the high-magnification areas. Age, P6. Scale bars, 100  $\mu$ m, 10  $\mu$ m, and 1  $\mu$ m respectively.

**(I-M)** Dendritic tuft volumes, number of PSD puncta, PSD puncta density, total PSD puncta area, and mean PSD puncta size were quantified. The results are shown by box plots, in which whiskers represent the maximum and minimum, boxes represent the inter-quartile range, and the horizontal lines represent the median. Each black dot represents individual mitral cells. n = 21, 21, and 23 cells, respectively. In *Bmpr2* KO and *Grin1* KO, 1/20 and 4/23 cells had multiple tufted structures, respectively. n.s, non-significant, \* p< 0.05, \*\* p<0.01, \*\*\* p<0.001 (One-way ANOVA with Tukey's post hoc test for **I, J, L, and M**, Kruskal-Wallis test with Dunn's multiple comparison test for **K**).

**(N)** A previous study reported the presence of "LIMK-binding regions" (751-813aa) (Lee-Hoeflich et al., 2004). However, BMPR-2 lacking this region (*Bmpr2 $\Delta$ 751-813aa*) rescued the phenotype of *Limk1* overexpression. This suggests that BMPR-2 inhibits LIMK with the tail domain but not at 751-813aa at least in mitral cells. Age, P6. Arrows and arrowheads indicate somata and primary dendrites, respectively. Scale bar, 100  $\mu$ m.

**(O)** Quantification of the number of glomeruli innervated per mitral cell. n, number of mitral cells. \*\*\*\* p<0.0001; n.s., non-significant ( $\chi^2$  test with Bonferroni correction, compared to the control).

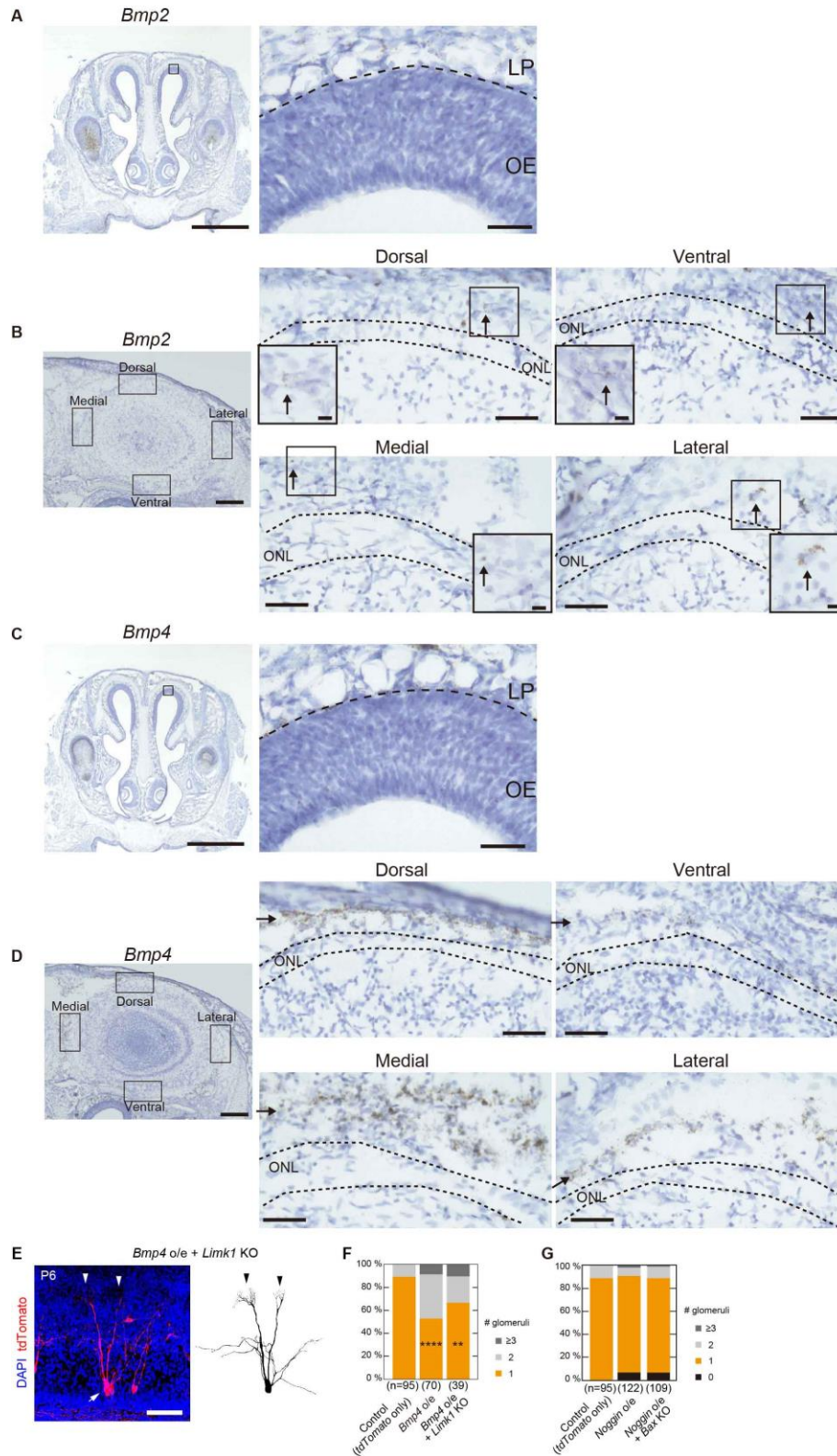


**Figure S3. Expression of *Bmp2* and *Bmp4*, Related to Figure 4.**

(A, B) Expression of *Bmp2* visualized by RNA scope combined with DAB staining. *Bmp2* expression was observed in the lamina propria (LP) but not in the OE. *Bmp2* was also expressed

on the OB surface, but at a lower level. Arrows indicate DAB signals. Insets show high magnification images of areas indicated by arrows.

**(C, D)** *Bmp4* expression was observed in the LP but not in the OE. *Bmp4* was also expressed on the OB surface, although the expression level was lower in the ventral part. Arrows indicate DAB signals.

Scale bars are 1 mm (A, C, left), 250  $\mu\text{m}$  (B, D, left), 50  $\mu\text{m}$  (middle and right), and 10  $\mu\text{m}$  (insets).

**(E)** *Bmp4* overexpression combined with *Limk1* KO. *Limk1* KO rescued the *Rac1* overexpression phenotype, but could not rescue *Bmp4* overexpression, suggesting that dendrite stabilization by BMPs is mediated via multiple signaling pathways. Age, P6. Arrows and arrowheads indicate somata and primary dendrites, respectively. Scale bar, 100  $\mu\text{m}$ .

**(F)** Quantification of the number of glomeruli innervated per mitral cell. n, number of mitral cells. \*\*  $p < 0.01$ ; \*\*\*\*  $p < 0.0001$  ( $\chi^2$  test with Bonferroni correction, vs control).

**(G)** *Noggin* o/e was combined with KO of *Bax* to suppress apoptosis. Quantification of the number of glomeruli innervated per mitral cell are shown. It is unlikely that mitral cells without primary dendrites are eliminated by apoptosis. n, number of mitral cells.

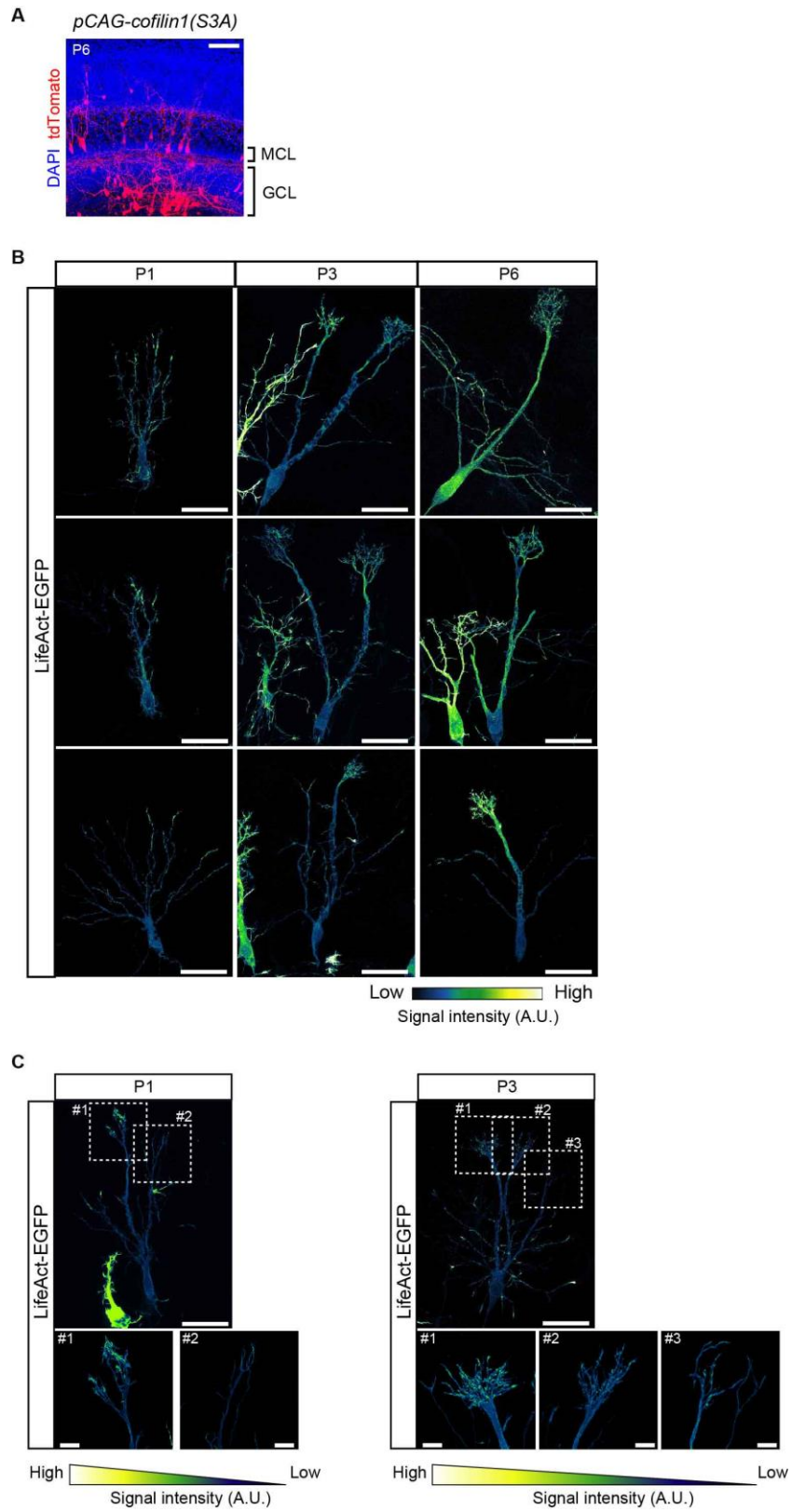


**Figure S4. Localization of F-actin, Related to Figure 7.**

**(A)** Overexpression of *cofilin1(S3A)* under a constitutively active CAG promoter. Many mitral cells were stacked in the granule cell layer (GCL), most likely due to a migration defect. MCL, mitral cell layer. Scale bar, 100  $\mu\text{m}$ .

**(B)** Additional examples of LifeAct-EGFP localization at different stages of dendrite remodeling. The signal intensity was adjusted to the brightest signal at the dendritic tufts. Scale bars are 50  $\mu\text{m}$ .

**(C)** In some mitral cells with multiple tufted dendrites, LifeAct signals were biased to one of multiple dendrites extending to the glomerular layer. In these examples, one of the dendritic tufts (#1) were brighter than the others. Here, the dendrite #1 had more developed tufted structure. This may indicate that F-actin formation is promoted in a prospective winner dendrite. Scale bars are 50  $\mu\text{m}$  (top) and 10  $\mu\text{m}$  (bottom).

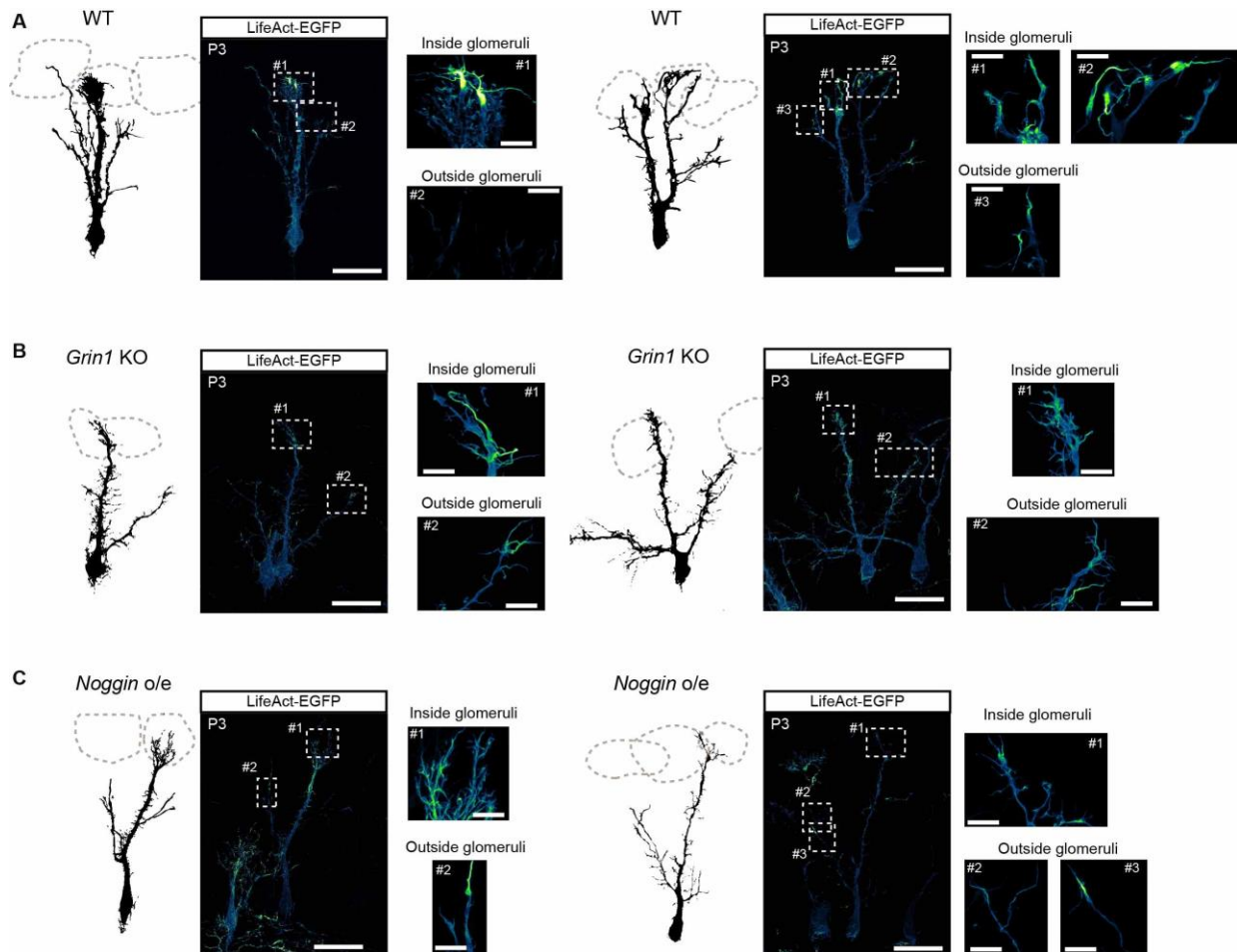


**Figure S5. Comparison of LifeAct signals between dendrites inside and outside glomeruli, Related to Figure 7.**

(A-C) Additional images of mitral cells extending dendrites inside and outside glomeruli. Traces are shown on the left. LifeAct signals were most prominent in dendritic terminals inside glomeruli in control, but not in *Grin1* KO and *Noggin* overexpression. Age, P3. Scale bars are 50  $\mu\text{m}$  (left) and 10  $\mu\text{m}$  (right).